Spring 2018

Comparing Three Pulsating Subdwarf B Stars Observed by Kepler in the Open Cluster NGC 6791

Joshua William Kern
Missouri State University, Kern28@live.missouristate.edu

COMPARING THREE PULSATING SUBDWARF B STARS OBSERVED BY *KEPLER* IN THE OPEN CLUSTER NGC 6791

A Masters Thesis

Presented to

The Graduate College of

Missouri State University

In Partial Fulfillment

Of the Requirements for the Degree

Master of Natural and Applied Science

By

Joshua W. Kern

May 2018

COMPARING THREE PULSATING SUBDWARF B STARS OBSERVED BY *KEPLER* IN THE OPEN CLUSTER NGC 6791

Physics, Astronomy, and Materials Science

Missouri State University, May 2018

Master of Natural and Applied Science

Joshua W. Kern

ABSTRACT

Using their entire *Kepler* data sets, I performed asteroseismic analyses and comparisons of three gravity (g-) mode pulsating subdwarf B (sdB) stars in the open cluster NGC 6791. I constructed light curves with a combination of long and short cadence data to span quarters 1 (Q01) through Q17 of KIC 2569576 (B3), KIC 2438324 (B4), and KIC 2437937 (B5). Rotationally induced g-mode frequency splittings were observed in each star allowing us to calculate rotation periods of 64.5 ± 8.2, 9.21 ± 0.18, and 91.3 ± 14.1 days for B3, B4, and B5, respectively. Using the observed ratio of the azimuthal multiplet components, I also constrained the inclination of the pulsation axis of each star and found that while B4 ($76° < i < 84°$) has an inclination close to equator-on, B3 ($i < 62°$) and B5 ($8° < i < 30°$) have inclinations which overlap with the preferred inclination of the cluster ($20° < i < 30°$). Asymptotic period spacings were determined in each star, and mode trapping was observed in one region of B3's asymptotic $l = 1$ sequence. From the full data sets of all three sdB stars, I detected a combined total of 65 pulsation frequencies of which I was able to identify 88% as $l \leq 2$ modes. Using these results and the cluster characteristics which include a common age, progenitor mass, and preferred inclinations for the sdB stars in NGC 6791, I discuss the comparison of B3, B4, and B5 to the known population of pulsating sdBs in order to give insight into their possible formation mechanisms and evolution.

KEYWORDS: subdwarf stars, oscillations, asteroseismology, Kepler, open cluster

This abstract is approved as to form and content

_____

Michael D. Reed
Chairperson, Advisory Committee
Missouri State University

COMPARING THREE PULSATING SUBDWARF B STARS OBSERVED BY *KEPLER* IN THE OPEN CLUSTER NGC 6791

By

Joshua W. Kern

A Masters Thesis
Submitted to the Graduate College
Of Missouri State University
In Partial Fulfillment of the Requirements
For the Degree of Master of Natural and Applied Science

May 2018

Approved:

_____
Michael Reed, PhD

_____
Robert Patterson, PhD

_____
Ridwan Sakidja, PhD

_____
Julie Masterson, PhD: Dean, Graduate College

TABLE OF CONTENTS

LIST OF TABLES

LIST OF FIGURES

INTRODUCTION

Stars form inside molecular clouds which can create tens to thousands of stars in what are called clusters. There are many types of clusters, however, open clusters are an example of a single population star cluster (Salaris, 2015). All of the stars in an open cluster form as the molecular cloud contracts, and are the same age and have the same initial metallicity. The cloud's angular momentum can also be transferred to the individual stars, establishing a preferred inclination (Corsaro et al., 2017).

SdB stars have been found in these types of clusters, including the old, metal-rich, open cluster NGC6791. There are 5 known sdB stars in the cluster including some pulsators (Kałuźny & Udalski, 1992; Liebert, Saffer, & Green, 1994; Pablo, Kawaler, & Green, 2011; Reed, Baran, Østensen, Telting, & O'Toole, 2012). Three of the pulsating sdB stars were observed during the main mission of the *Kepler* space telescope; KIC 2569576 (B3), KIC 2438324 (B4), and KIC 2437937 (B5) (Pablo et al., 2011; Reed et al., 2012). Since the lifetime of a star is directly tied to its mass, it implies that the progenitor mass of any sdB star in NGC 6791 must be the same. This means that B3, B4, and B5 give us the unique opportunity to compare three pulsating sdB stars which have roughly the same age, progenitor mass, initial metallicity, and preferred inclination. Any differences in their current asteroseismic and atmospheric properties are indicators of possible differing formation mechanisms or bulk properties such as core or envelope mass.

The following sections include a description of sdB stars, stellar evolution, asteroseismology, and the *Kepler* mission. I then present our data processing, analyses,

and the results of applying known asteroseismological tools to the entire *Kepler* data sets of B3, B4, and B5. Finally, I discuss the similarities and differences between the three stars, and how they compare to the properties of other known *Kepler* sdB stars, as well as our knowledge of sdB evolution in general.

Subdwarf B Stars

Subdwarf B stars were discovered by Humason and Zwicky (1947) during a photometric survey of the North Galactic pole. With a focus strictly on blue objects in the northern galactic hemisphere, the Palomar-Green (PG) survey was the first large discovery of sdB stars (Green, Schmidt, & Liebert, 1986). Many surveys followed, including the Kitt Peak-Downes survey of the galactic plane (Downes, 1986), the Edinburgh-Cape and the Hamburg European Space Organization surveys of the southern sky (Stobie et al., 1997; Wisotzki, Koehler, Groote, & Reimers, 1996), and the all sky Sloan Digital Sky survey (SDSS), which have aided in the discovery of sdB stars.

Spectroscopically, a typical sdB or sdO star's spectrum is dominated by strong hydrogen lines and weak helium lines. The weak helium lines are due to a helium deficient envelope which is caused by diffusive processes (Greenstein, 1967). The envelope contains primarily hydrogen, however, at 10^{-4} $M_{\odot}$ it is too thin to sustain hydrogen shell fusion. Nearly 10% of sdB/sdO stars have strong helium lines in their spectra, and are thus referred to as He-sdBs and He-sdOs (Green et al., 1986).

The effective temperatures of sdB stars range from 20,000 to 40,000 Kelvin (K) with log *g* (cgs) values ranging from 4.8 to 6.0 dex (Greenstein & Sargent, 1974). These stars are on the HR-diagram below the upper main sequence and above the white dwarf

cooling track (WDCT); an example showing where these stars fall on an HR-diagram is shown in Figure 1. Heber et al. (Heber, Hunger, Jonas, & Kudritzki 1984; Heber, 1986) showed these stars to be extreme horizontal branch (EHB) stars and thus core helium-fusing stars.

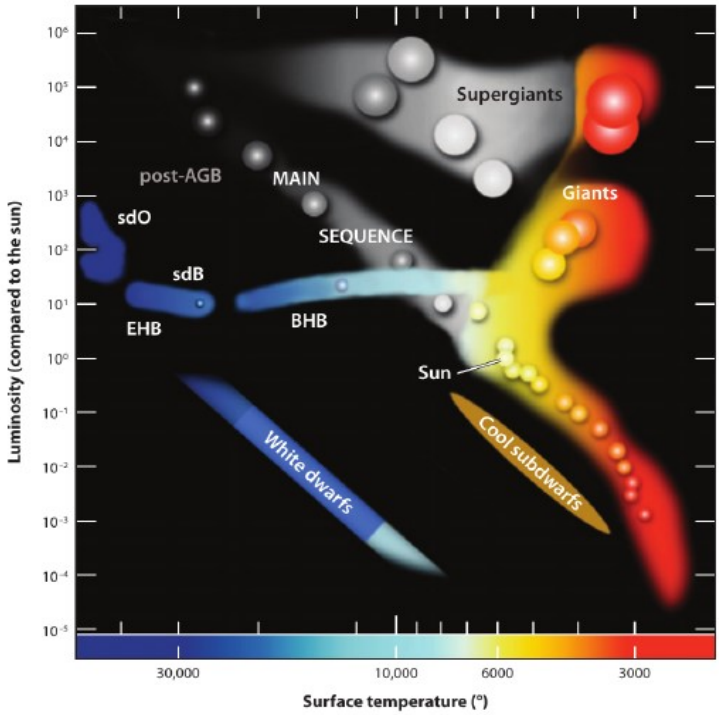

Figure 1: HR-Diagram depicting the position of sdB stars on the EHB. *Credit: Heber, 2009*

Importantly, the helium flash, which is the onset of helium fusion, generally happens at the same core mass ($M_c \approx 0.47\ M_\odot$) for low-mass stars, which in this thesis is defined as stars with masses less than about 2 $M_\odot$. Based on the masses of 22 stars derived from asteroseismology and eclipsing binary systems, an empirical distribution of sdB masses was determined by Fontaine et al. (2012) and Van Grootel, Charpinet, Fontaine, Brassard, and Green (2014). Their results agree with the predictions from

stellar evolution where the average sdB mass from this small sample was found to be 0.470 $M_{\odot}$ (Fontaine et al., 2012; Van Grootel, Charpinet, Fontaine, Brassard, & Green, 2014). The mass range from 0.439 to 0.501 $M_{\odot}$ contains 68.3% of the stars with a histogram of the data presented in Figure 2. Since sdB stars are EHB stars and thus undergo helium fusion, this shows that sdB stars are the remnant cores of red giant (RG) stars that have almost completely lost their envelope. The envelope ejection and the onset of helium fusion must be nearly simultaneous as the envelope is necessary for helium ignition, yet mass loss is not observed on the horizontal branch (HB). The cores of sdB stars do not get hot enough to do carbon fusion, so the sdB star will evolve into a carbon oxygen-white dwarf (CO-WD) and end its life on the WDCT.

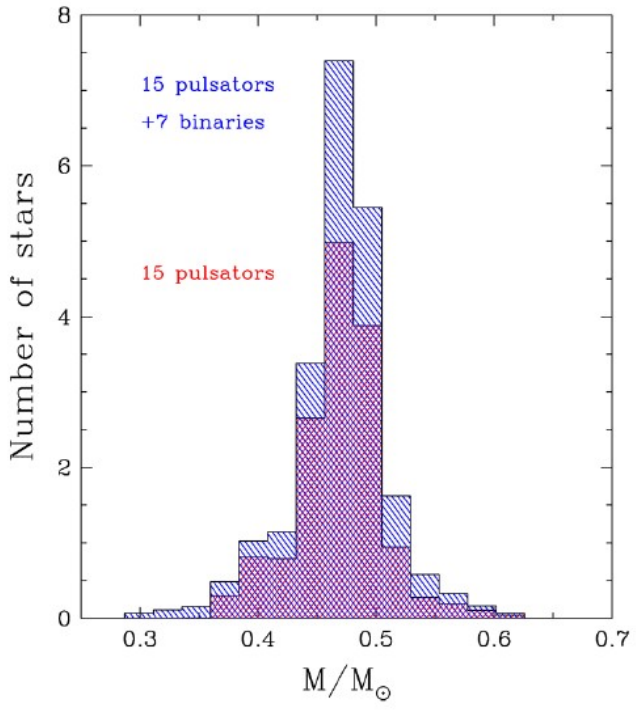

Figure 2: The empirical mass distribution of 22 sdB stars as determined by Fontaine et al. 2012. The blue hatched area represents the entire set of stars, whereas the red hatched area indicates only the pulsators. *Credit: Fontaine et al., 2012*

In general, sdB stars are post-main sequence, helium fusing stars which are characteristic of the late evolutionary stages of low-mass progenitor stars. Next, I will explore the details of where sdB stars fit into stellar evolution by discussing the evolution of a 1 $M_{\odot}$ star.

Stellar Evolution

In this section I describe the evolution of a 1 $M_{\odot}$ star with a solar-like chemical abundance (i.e. X = 0.7, Y = 0.28, Z = 0.02) based on Heber (2016) and Prialnik (2010) along with a discussion of sdB formation channels due to binary interactions.

Main Sequence. A 1 $M_{\odot}$ star on the main sequence fuses hydrogen into helium. As gravity attempts to contract the star, the gas pressure caused by hydrogen fusion and smaller thermal energies counterbalance the inward force. The star is in a state of hydrostatic and thermal equilibrium due to the stable, sustained hydrogen fusion in the core. Hydrogen fusion is sustained in two ways via the proton-proton (p-p) chain or the carbon-nitrogen-oxygen (CNO) cycle.

For low-mass stars, the primary form of energy generation is through the p-p chain. In general, the p-p chain fuses four protons through a series of steps into a helium nucleus. This produces a sufficient amount of energy that a 1 $M_{\odot}$ star would have a main sequence lifetime of roughly 9 billion years. The star leaves the main sequence after the central hydrogen is used up, and observationally, the star's envelope cools slightly.

Post-Main Sequence. As the star enters the subgiant phase the core contracts, the envelope expands, and the shell of hydrogen fusion gradually thins. As the envelope expands, it cools and becomes more opaque to radiation generated in the core. As the

core continues to contract, it reaches a state where electron degeneracy begins to counterbalance gravity of the inert helium core. At this point, the star is at the base of the RGB and the outer envelope becomes convective.

As the star proceeds up the RGB, the convection zone in the envelope reaches deeper toward the core, eventually bringing up by-products from the hydrogen shell fusion in an event known as the first dredge-up. The envelope continues to expand as the star traverses up the RGB where it reaches a point that it becomes nearly detached from the core. Since the envelope is very loosely bound, stellar winds can cause mass loss which increases as the star reaches the tip of the RGB.

Helium Flash. It is near the tip of the RGB when the core of the star has contracted enough that temperatures reach nearly 10^8 K and helium fusion ignites. For low-mass stars, the helium fusion ignition happens at a common core mass of $M_c \approx 0.47$ $M_\odot$ and under degenerate conditions in which pressure and temperature are decoupled. Since energy generation rates are very temperature dependent, helium fusion that takes place in a degenerate core is unstable. Helium fusion causes an increase in temperature which allows even more helium to fuse. The increase in temperature does not create an increase in pressure, so the core does not expand as it gets hotter. This creates a thermonuclear runaway in the core which produces excessive amounts of energy that are absorbed by the outer portion of the core and the non-degenerate layers around the core in an event known as the helium flash. Almost all of the energy produced from the helium flash is absorbed by the opaque outer layers, effectively hiding the event from observers.

Horizontal Branch and Beyond. After the helium flash the core is undergoing stable helium fusion and moves to the HB. Since most stars on the HB have a constant core mass of ~0.47 $M_{\odot}$, the distribution of stars on the HB can be explained by varying envelope masses which decrease as you move to higher temperatures. For some stars with increased mass loss on the RGB, they lose nearly their entire envelopes and end up being very hot, extreme horizontal branch (EHB) stars; an example of which is an sdB star.

For sdB star formation, the progenitor must lose nearly its entire envelope mass near the tip of the RGB in simultaneity with helium-fusion ignition. Possible mechanisms for single sdB star formation include enhanced stellar wind mass loss (D'Cruz, Dorman, Rood, & O'Connell, 1996), envelope stripping in dense clusters (Marietta et al. 2000), and white dwarf mergers. Other methods of mass loss involve binary systems which are discussed in the next section.

The lifetime of any star on the HB is on the order of 10^8 years and ends once helium fusion has been exhausted. For typical stellar evolution of a 1 $M_{\odot}$ star, the inert CO core begins to contract, helium fusion is pushed into a shell surrounded by the thin hydrogen fusing shell and the outer envelope. As the core contracts, the envelope expands and the star traverses the AGB. Over the course of roughly 10,000 years, stellar winds and thermal pulses on the AGB can completely strip the envelope, creating a planetary nebula, and leaving only the degenerate CO core; a CO-WD.

However, EHB stars (e.g. sdB stars) have too thin of envelopes to have H-shell nuclear fusion. When these stars run out of He in the core, fusion gets pushed into a shell causing the layers on top of this shell to heat and expand. If any remaining H is in the

envelope, the star could undergo H-shell fusion for a very short time. These stars end their lives as CO-WDs on the WDCT.

Subdwarf B Formation

Binary Stars. Other than enhanced mass loss at the tip of the RGB, binary-interaction processes can also explain the formation of sdB stars. Many sdB stars reside in short-period (0.5 to 30 day) binary systems with white-dwarfs or main sequence M-type stars, as well as long-period (700 to 1200 day) binaries with main sequence F-, G-or K-type stars (Copperwheat, Morales-Reda, Marsh, Maxted, & Heber, 2011; Vos et al., 2013). In fact, half to two-thirds of sdB stars are in binary systems meaning that the majority of sdBs form due to binary-interaction processes (Reed & Stiening, 2004; Copperwheat et al., 2011; Maxted, Heber, Marsh, & North, 2001). A combination of common envelope (CE) evolution and Roche Lobe overflow (RLOF) can explain the formation of sdBs in both short and long-period binaries.

Formation Channels. In a binary star system, a Roche lobe is the tear-drop shaped, equipotential surface surrounding either star within which matter is gravitationally bound to the star. If a star expands to fill this Roche lobe, then its mass can be transferred to the companion.

Consider a close binary system consisting of two main sequence stars (middle panels of Figure 3). As one of the stars leaves the MS and moves to the RGB, the star begins to swell. It expands to a point where it fills its Roche lobe near the tip of the RGB, and mass transfer begins. If the mass transfer rate is too high, then the companion cannot accrete the material and the RLOF is unstable. The excess material fills the Roche lobe of

the companion, and a common envelope can form. The common envelope exerts a frictional drag on the orbiting stars causing the envelope to heat up, consequently ejecting the material, and the two stars re-emerge in a short-period binary. Since the CE phase is short lived and the companion cannot accrete much of the envelope mass, the companion remains relatively unchanged and what is left behind is an sdB + M binary.

Now, consider a wide binary system consisting of two main sequence stars (right panels of Figure 3). The difference between this formation channel and the previous scenario is that a dual-MS wide binary system can sustain stable RLOF as one of the partners expands on the RGB. From this, the resultant system would be a long-period sdB + MS binary.

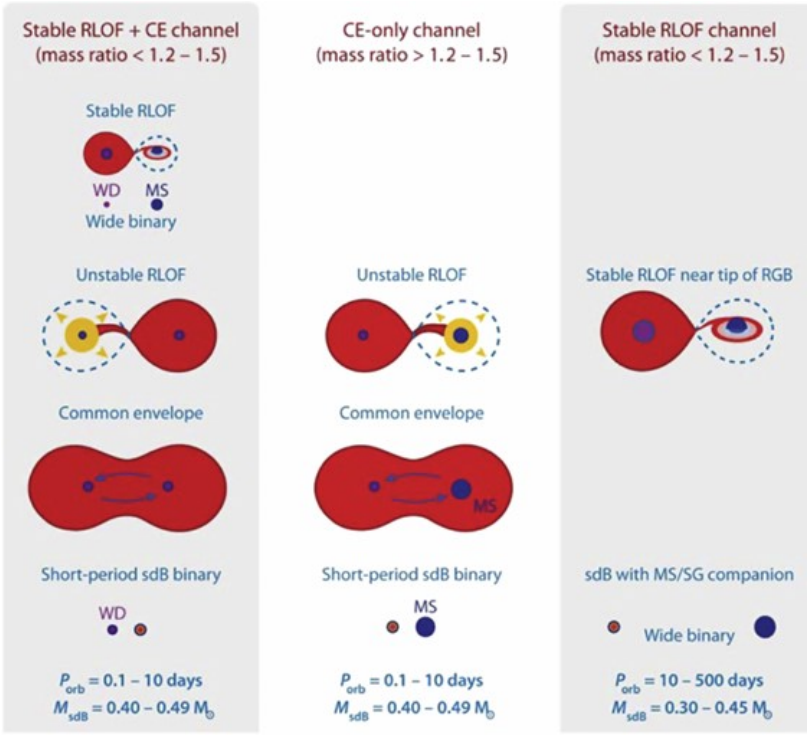

Figure 3: A schematic of sdB formation through three binary-interaction scenarios (Stable RLOF + CE, CE-only, and Stable RLOF only). Note that either channel with a CE phase results in a short-period sdB binary system. *Credit: Heber, 2009*

However, this system could continue evolving (left panels of Figure 3). The sdB exhausts its core helium much faster than the hydrogen in the core of the MS star becoming a WD. If the WD + MS binary now goes through a second RLOF phase, albeit unstable, the system could enter a subsequent CE phase. The outcome of this CE phase is a short-period sdB + WD binary system.

Subdwarf B Evolution

All the previously discussed formation mechanisms create sdB stars that have very low density hydrogen envelopes which are doing core helium fusion as they appear on the zero-age extreme horizontal branch (ZAEHB, shown in Figure 4). The sdB star will spend its life on the EHB doing core helium fusion (roughly 10^8 years depending on core overshooting; Schindler, Green, & Arnett, 2014).

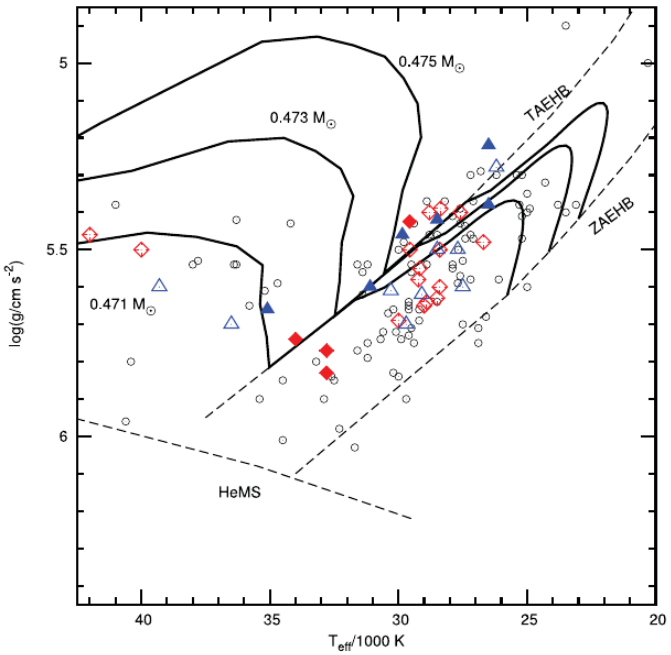

Figure 4: Evolutionary tracks of sdB stars plotted on a distribution of sdB stars in close binaries from Kupfer et al. 2015. Filled points are pulsators, eclipsing systems are red squares, and non-eclipsing systems are blue triangles. *Credit: Heber, 2016*

After the core helium is exhausted, the star will begin a phase of shell helium fusion, which will make the star expand slightly and, consequently, create lower surface gravities. Shell helium exhaustion occurs when the star has reached the terminal-age extreme horizontal branch (TAEHB, shown in Figure 4). After total helium exhaustion, sdBs do not have sufficient temperatures to ignite carbon fusion, so the star evolves off the TAEHB and ends its life on the WDCT.

Pulsating Subdwarf B Stars

Low-amplitude, short-period (a few minutes) pulsations in sdB stars were discovered by Kilkenny, Koen, O'Donoghue, and Stobie in 1997. Long-period (45 minutes to 2 hours) pulsations were discovered in sdB stars by Green et al. in 2003. Both types were predicted in theory to be non-radial pulsations driven by an iron opacity bump (Charpinet, Fontaine, Brassard, & Dorman, 1996; Charpinet et al., 1997; Fontaine et al., 2003). Stars with short-period pulsations are pressure (p-) mode pulsators, whereas stars with long-period pulsations are gravity (g-) mode pulsators. These two types of pulsators led to the distinction of two sdBV types: V361 Hya stars (p-mode pulsators) and V1093 Her stars (g-mode pulsators).

As seen in Figure 5, V361 Hya stars (*p* modes) are hotter ($28{,}000 < T_{eff} < 35{,}000$ K) and have slightly higher surface gravities ($\log g > 5.55$ dex) compared to V1093 Her stars (*g* modes). The distinction between p- and g-mode pulsations is that *p* modes are acoustic waves that propagate predominantly in the envelope of the star, whereas gravity waves (*g* modes) penetrate all the way to the convective core. As expected, so-called hybrid pulsators, exhibit both p- and g-mode pulsations (Schuh et al., 2006). Hybrid stars

allow for a unique opportunity to use asteroseismology to probe the core and the envelope of the star simultaneously.

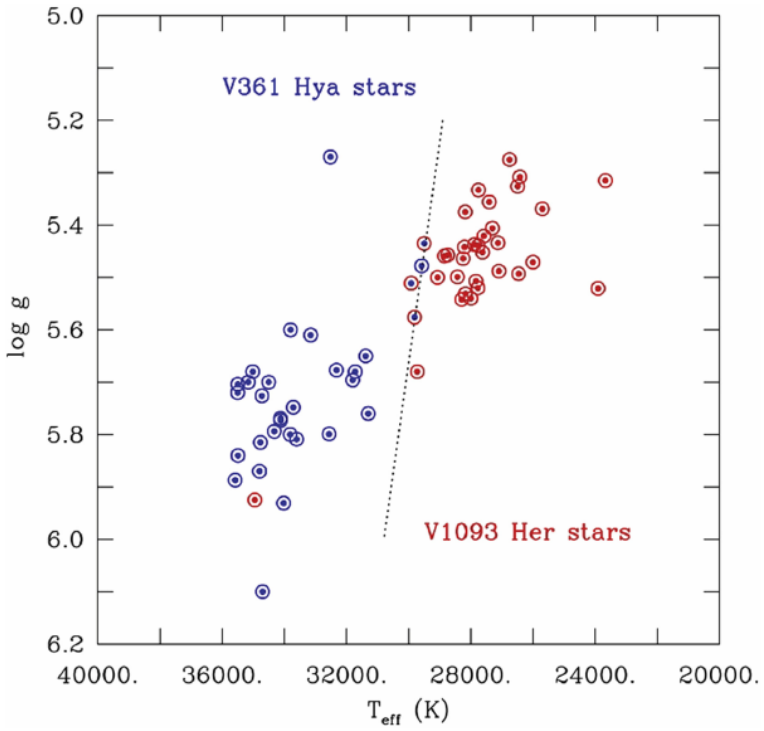

Figure 5: 61 SdB pulsators plotted on a log *g*/effective temperature graph; 28 *p* modes, 30 *g* modes, and 3 hybrid pulsators. Notice the dichotomy of p- to g-mode pulsators with three hybrids lying on the boundary at ~30,000 K. *Credit: Green et al., 2011*

Asteroseismology

In general, asteroseismology uses the propagation of waves throughout a star to determine its structure. The tools of asteroseismology are used to determine pulsation mode identifications, which can be used to derive rotation periods and discern structural boundaries. An illustration depicting these pulsations and their propagation through a solar-like interior is shown in Figure 6.

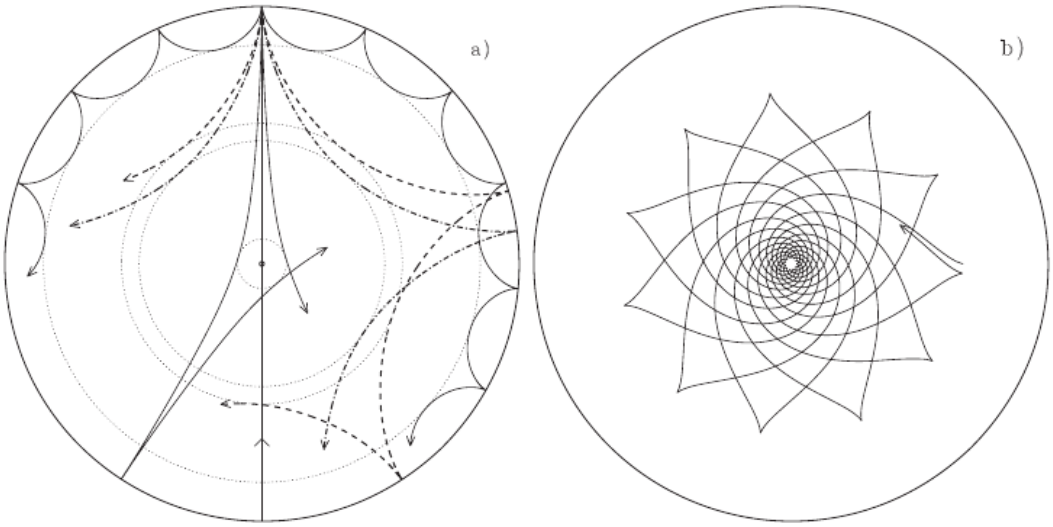

Figure 6: Propagation of pressure (interior a) and gravity (interior b) mode waves throughout a cross-sectional solar interior. The pressure waves represent a pulsation frequency of 3000 μHz with degrees l = 2, 20, 25, and 75 which correspond to the rays of decreasing penetration depth. Similarly for interior b, the gravity mode illustrated is of degree l = 5 with pulsation frequency of 190 μHz. For completeness, a radial pulsation is plotted as the line passing through the center of interior a. *Credit: Cunha et al., 2007*

Pulsation modes can be characterized by three quantum numbers: *n, l,* and *m.* The radial nodes are denoted by *n,* the total surface nodes are given by *l,* and the surface nodes passing through the pulsation axis of the star are denoted by *m.* Where *l* and *m* are observable quantities, the exact value of *n* is not explicitly identifiable due to the observational uncertainty in the position of the radial fundamental node (n = 0; marks the transition from g- to p-mode pulsations).

Asymptotic Period Spacing. In the case of a completely homogeneous stellar interior and in the asymptotic limit of $n >> l$, g-mode pulsations exhibit even period spacings with sequences given by

$$\Pi_{\ell,n} = \frac{\Pi_o}{\sqrt{\ell(\ell+1)}} n + \epsilon, \qquad 1$$

where Π_o is the fundamental radial period and ϵ is a constant encompassing details of stellar structure (Unno, Osaki, Ando, & Shibahashi, 1979; Aerts, Christensen-Dalsgaard, & Kurtz, 2010). The spacing between consecutive *n*-overtones for a given *l*-value is

$$\Delta \Pi_\ell = \frac{\Pi_o}{\sqrt{\ell(\ell+1)}}. \qquad 2$$

Predominantly, $l = 1$ and 2 pulsation modes are observed, because of geometric cancellation (Pesnell, 1985), which is caused by viewing nearly-equal areas of brighter and dimmer regions. The explicit relationship between $l = 1$ and 2 modes is

$$\Delta \Pi_{\ell=2} = \frac{\Delta \Pi_{\ell=1}}{\sqrt{3}} \qquad 3$$

Kolmogorov-Smirnov Test. Reed et al. (2011) determined asymptotic period spacing relationships for 13 sdB stars observed by the *Kepler* spacecraft. They used period transforms (PTs), the Kolmogorov-Smirnov (KS) test, and linear least squares fitting to determine the period sequences. The sequences were determined to be significant based on Monte Carlo testing. In all 13 sdB stars they detected the $l = 1$ period spacing near 250 seconds, while the $l = 2$ period spacing near 145 seconds was detected in roughly half of the stars; a subsample of these is shown in Figure 7.

Échelle Diagrams and Mode Trapping. The tools used to reveal period spacings do not discern which pulsations belong to a specific sequence. To do so, échelle diagrams are used which plot the period modulo against period where pulsations intrinsic to a sequence align vertically on the plot. An example of an échelle diagram for the $l = 1$ and

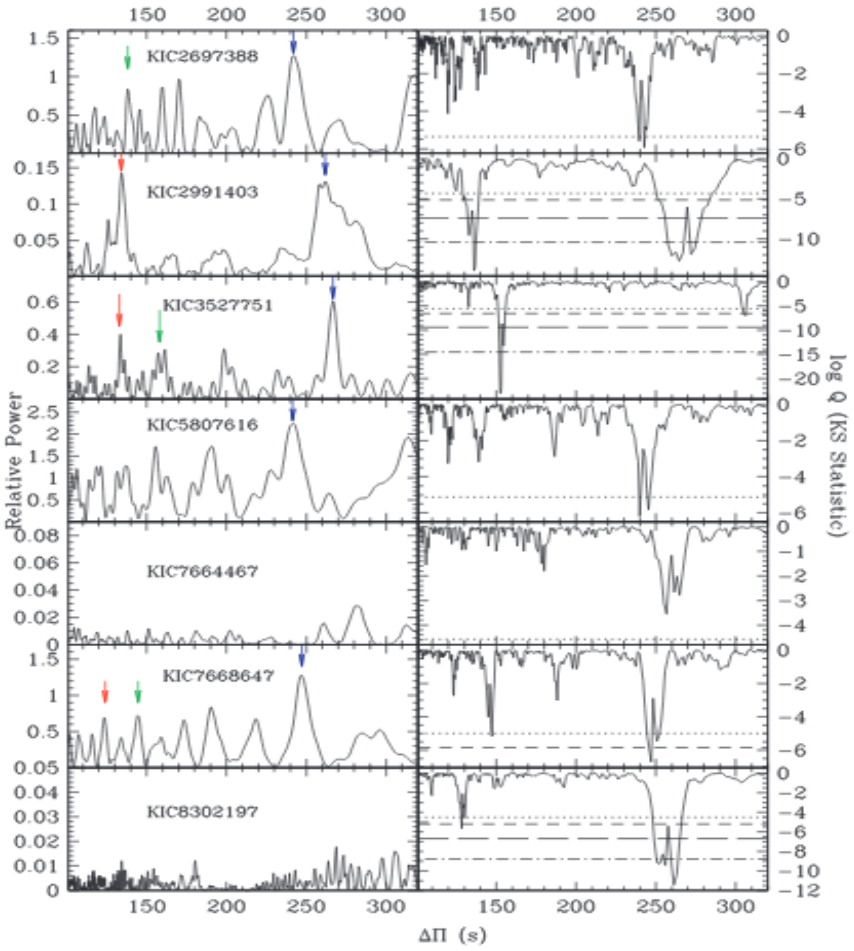

Figure 7: The PTs (left panels) and KS tests (right panels) of 7 sdB pulsators. Blue, green, and red arrows in the PTs indicate the $l = 1$ spacings, $l = 2$ spacings, and their aliases, respectively. The various dotted, short dashed, long dashed, and dot-dashed lines in the KS plots indicate confidence intervals of 90%, 95%, 99%, and 99.9%, respectively. *Credit: Reed et al., 2011*

2 pulsations in KIC 10670103 is presented in Figure 8. Échelle diagrams and linear regression fittings have been used to determine pulsation sequences (Reed et al., 2011).

If the star were completely homogeneous, these pulsations would have a very well-defined period spacing, and the sequence would align exactly vertically on the échelle diagram. However, slight deviations from the sequence and trapped modes have

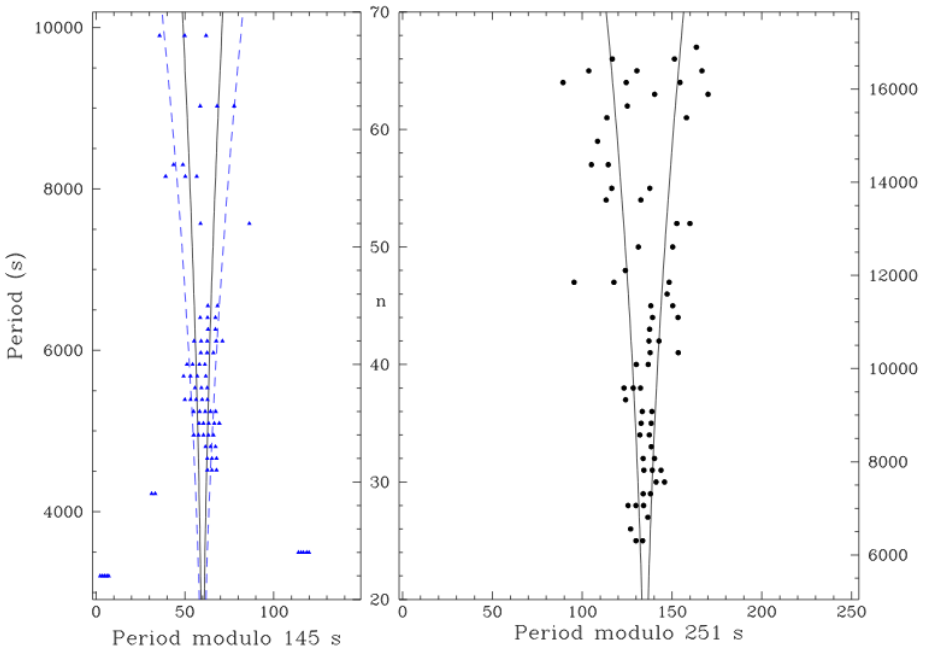

Figure 8: An échelle diagram for KIC 10670103 plotting the $l = 1$ (right panel) and $l = 2$ (left panel) period modulo for only the identified modes of the corresponding degree l. The solid lines indicate the calculated position of the $m = \pm 1$ components based on the frequency splitting of KIC 10670103. The dashed lines correspond to the $m = \pm 2$ components. *Credit: Reed et al., 2014*

been observed (Østensen et al., 2014; Foster, Reed, Telting, Østensen, & Baran, 2015; Kern, Reed, Baran, Østensen, & Telting, 2017). These smaller deviations from the asymptotic period spacing are indicative of changes in the chemical composition of the star (Charpinet, Fontaine, Brassard, & Dorman, 2002). Trapped modes may occur at the C-O/He transition layer as the result of convective overshoot (Constantino, Campbell, Christensen-Dalsgaard, Lattanzio, & Stello, 2015; Ghasemi, Moravveji, Aerts, Safari, & Vuckovic, 2017). If mode trapping occurs at a specific radial node (n), then it will affect all pulsation modes regardless of their degree l. Conversion to reduced period, Π, by multiplying by $(l\,(l+1))^{1/2}$, makes the degrees degenerate. In this modified échelle diagram, the degenerate degrees align with a common spacing (~350 seconds) and

trapped modes stand out as deep troughs in the plot; an example of which is given in Figure 9.

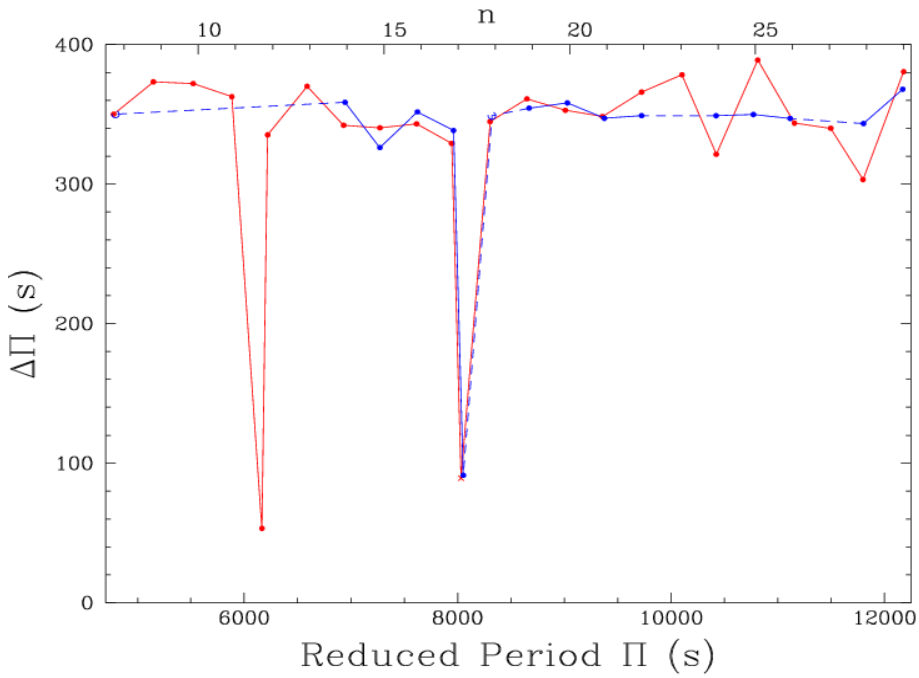

Figure 9: Reduced period plot of KIC 11558725 indicating trapped modes at ~n = 12 and 17. The blue and red points/lines represent the l = 1 and 2 sequences, respectively. Solid lines correspond to consecutive radial nodes, whereas the dashed lines represent missing nodes. *Credit: Kern, Reed, Baran, Telting, and Østensen, 2018*

Rotationally Induced Frequency Splittings. If a star completes multiple rotations during observations with a rotation frequency Ω, then frequency multiplets may form; examples of l = 2 multiplets from the sdB star KIC 10670103 are given in Figure 10 (Reed et al., 2014). When all of the components in the multiplet are driven, it will have $2l + 1$ peaks separated with a frequency splitting given by

$$\Delta\nu = \Delta m \Omega \left(1 - C_{n,\ell}\right), \qquad 4$$

where Δm is the difference in azimuthal order. The Ledoux constant, $C_{n,l}$, for *p* modes in sdB stars is effectively zero (Charpinet et al., 2002), however, for *g* modes it is given by

$$C_{n,\ell} \approx \frac{1}{\ell\,(\ell+1)} \qquad 5$$

(Ledoux et al., 1951; Aerts et al., 2010).

Thus, the characteristic even splittings of pulsation multiplets allows for the derivation of rotation rates for the location in the star in which the pulsation occurs. Since *p* and *g* modes propagate from different, but overlapping, regions of the stellar interior, hybrid pulsators allow for the determination of solid-body or radial differential rotation which has been done for sdB stars KIC 2697388 (solid-body; Kern et al., 2017), KIC 11558725 (solid-body; Kern, Reed, Baran, Telting, & Østensen, 2018), KIC 3527751 (radial differential; Foster et al., 2015), and EPIC 211779126 (radial differential; Baran, Reed, Østensen, Telting, & Jeffery, 2017). Typical rotation periods for sdB stars are in the range of 10 to 100 days (Reed et al., 2014). Tidal synchronization can now be determined by directly comparing the rotation period with the binary period.

From theory, tidal synchronization timescales depend upon the gravitational interaction of the two bodies from which you would expect higher probabilities of synchronization in binaries with short orbital periods (Pablo et al. 2011). Tidal synchronization has been determined in short-period sdB binaries using ground-based observations of the p-mode pulsators NY Vir (orbital period P = 2.42 hours; Charpinet et al., 2008) and Feige 48 (P = 8.25 hours; Latour et al., 2014). Both of which were found to have solid-body rotation at least for the outer portion of the star. Synchronization has

also been seen in a short-period binary observed using *Kepler* (Østensen et al., 2010a). However, the *Kepler* spacecraft has revealed numerous sub-synchronous binaries with orbital periods greater than 8 hours (Pablo et al., 2011; Kawaler et al., 2010; Telting et al., 2010; Reed et al., 2016).

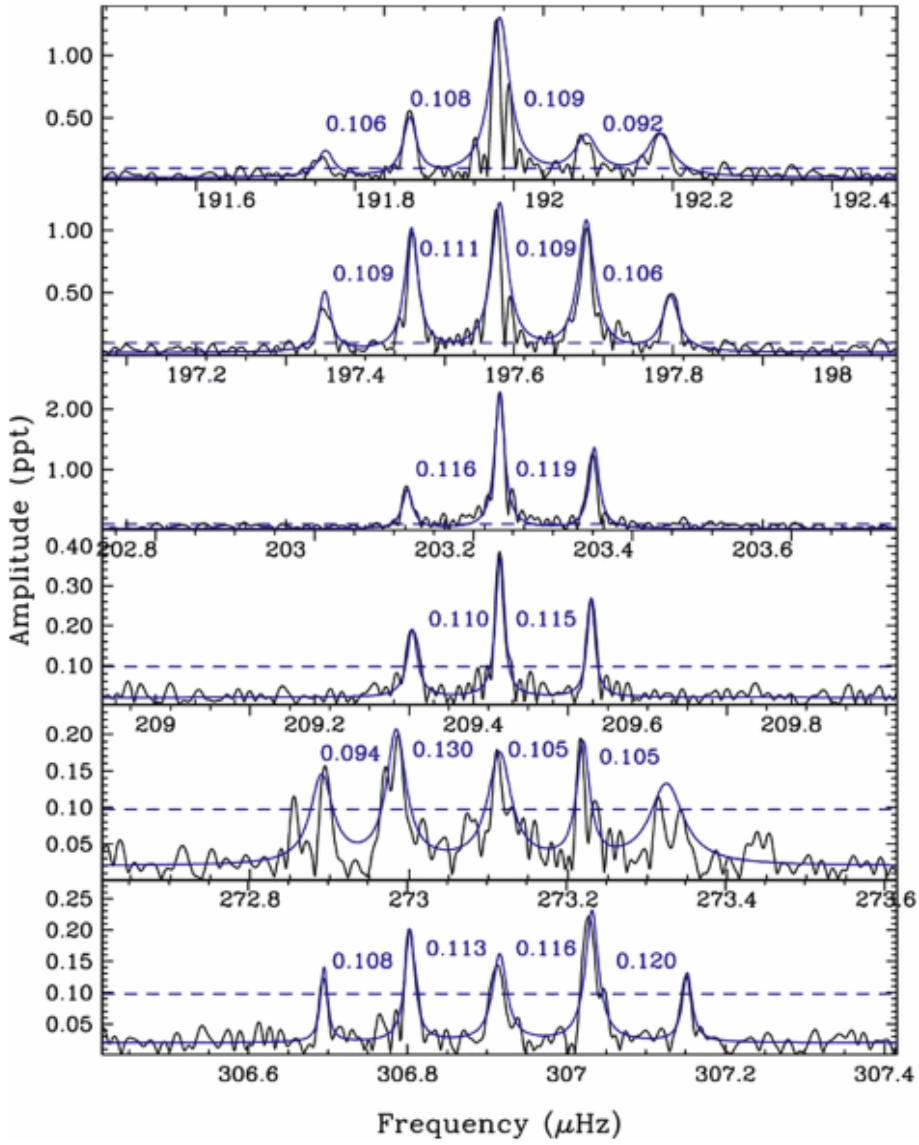

Figure 10: Examples of $l = 2$ multiplets from KIC 10670103 with frequency splittings ~0.110 μHz. *Credit: Reed et al., 2014*

Kepler Space Telescope: Science Goals and Mission Design

Tremendous progress in the field of asteroseismology is due to the *Kepler* space mission and its ability to obtain precise photometric light curves over extended periods of time. *Kepler* data are unique in their duration (~1500 days), duty cycle (~85%), and lack of atmospheric obscuration. This precision translates to a frequency resolution roughly an order of magnitude better than its French predecessor, CoRoT: COnvection ROtation et Transits planétaires (Bordé, Rouan, & Leger, 2003). Similar to CoRoT, *Kepler's* main focus is the detection of exoplanets (specifically Earth-sized) with a lesser emphasis on stellar astrophysics. However, compared to CoRoT, the *Kepler* spacecraft's collecting area is 9.25 times greater (Koch et al., 2010). Even with a lesser emphasis on stellar astrophysics, because the spacecraft observed such a wide variety of stars, *Kepler* data has greatly benefited a swath of fields outside of exoplanet research including asteroseismology. A thorough overview of the *Kepler* spacecraft's mission design is presented by Koch et al. (2010) and are summarized in the following subsections.

Duration. The *Kepler* spacecraft observes exoplanets via transit photometry (Kasting, Whitmire, & Reynolds, 1993). The transit method of detecting exoplanets allows for the determination of radii relative to its host star and orbital period. A minimum of three transits with consistent depth, duration, and period must be observed in order to have confidence that the signal is indeed a planet. For Earth-Sun analogs the orbital period is one year, therefore the duration of the mission was designed to last a minimum of three years. The original *Kepler* mission observed from May 12, 2009 to May 11, 2013. Each year is broken up into four quarters. With every solstice and equinox, the spacecraft rotates 90º along its focal plane accumulating four rotations every

year which are necessary to orient the sunshade (shown in Figure 11) and solar arrays toward the Sun.

Photometry. To detect transits from Earth-Sun analogs, the photometric precision must be able to detect a change in luminosity proportional to the ratio of their areas; 84 parts-per-million (ppm). If an Earth-Sun analog's orbital plane is completely perpendicular to our line of sight, its transit will last 13 hours. Thus, the *Kepler* mission was designed to detect a signal of 84 ppm with a transit duration half of that of the Earth-Sun system.

The level of precision needed to complete *Kepler's* science goals are achieved with a ~1 m Schmidt telescope (0.95 m aperture), ~105 degree^2 field-of-view (FOV), and a 55° solar avoidance angle in an Earth-trailing heliocentric orbit (ETHO). An ETHO has many advantages compared to a low-Earth orbit, mainly due to the lack of disturbing torques which allows for stable, precise photometry. A non-Earth orbit space-based telescope has the advantages of being able to observe continuously, as there is no daytime, requires no atmospheric corrections, and has a large zone available for continuous viewing. A Schmidt telescope allows for a large FOV, and creates a curved focal surface. Therefore the 42 thin, back-illuminated charge-coupled device (CCD) modules (from e2v Technologies) are mounted on a curved surface, with sapphire field-flattening lenses (FFLs) and four guidance sensor CCDs; these are shown in Figure 11, as well as a cross-sectional view of the photometer. To maximize the signal-to-noise (S/N), the spectral bandpass spans from 423 nm (blue cutoff; chosen to avoid Ca II H and K lines) to 897 nm (red cutoff; chosen to avoid fringing due to internal reflection in the CCDs).

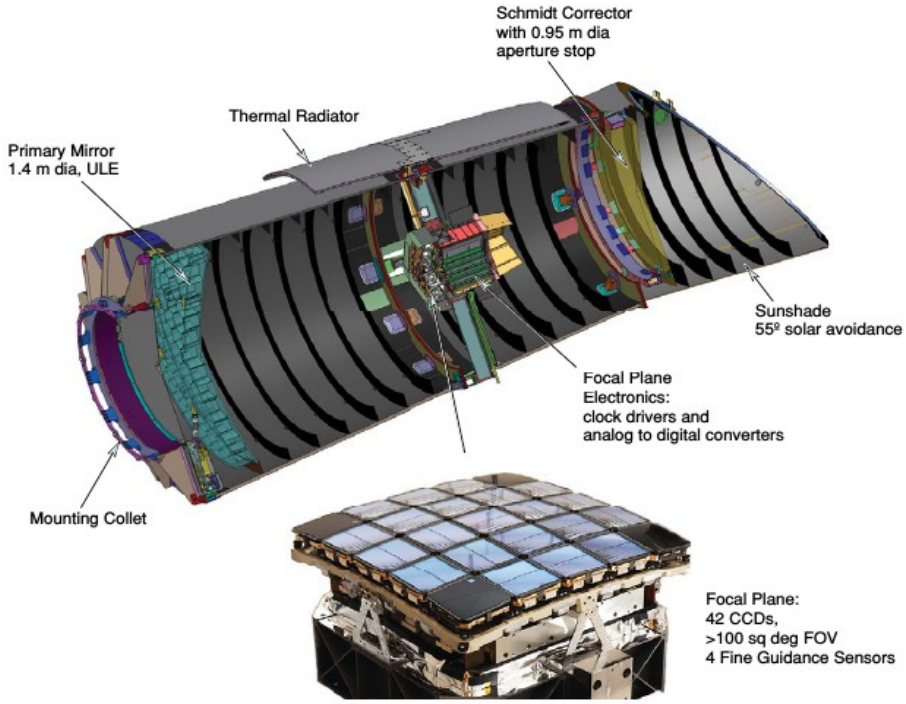

Figure 11: Cross-sectional view of the *Kepler* spacecraft photometer, as well as a picture of the focal plane which holds the 42 CCDs. *Credit: Koch et al., 2010*

To reduce photometric noise the CCDs are operated below -85°C and integration times are 6.02 seconds. Readouts from the CCDs are stacked into varying data cadences. Long cadence (LC) data sums 270 readouts for an integration time of ~30 minutes, whereas short cadence (SC) data sums 9 readouts for an integration time of ~1 minute. After the readouts are stacked for either cadence, only the pixels of interest are extracted from the full-field images (which are also recorded, calibrated, and archived once per month). Where LC data are used to detect planetary transits, SC data are used to improve transit timing and have also allowed for precision asteroseismology of sdB stars (Østensen et al., 2010b).

Star Field. The *Kepler* star field is 13.5° above the galactic plane in the constellations Cygnus and Lyra. It is centered on right ascension (R. A.) = 19h 22m 40s and declination (Dec.) = 44° 30' 00", and was chosen due to its rich star field. The field-of-view is roughly 10 degrees on each side and is shown in Figure 12. The orientation of the focal plane minimizes the number of bright stars on the CCDs which cause over-saturation and loss of usable pixels. Only 12 stars with a V = 6 or brighter were directly on the CCDs, and the majority of the stars observed have V > 10. Each observed star is given a Kepler Input Catalog (KIC) number for distinction.

Four gyroscopic reaction wheels on board are responsible for stabilizing the spacecraft's pointing. However, in May 2013 the spacecraft lost a second reaction wheel and was unable to continuously monitor the field (Van Cleve et al., 2016). This led to a secondary mission, the K2 mission, which observes a star field for ~80 days continuously before it must change direction due to limiting solar angle constraints. The remainder of this thesis will focus on the open cluster NGC 6791 which was observed by *Kepler* during its main mission (shown in Figure 12), and three sdBV stars which reside in it; KIC 2569576 (B3), KIC 2438324 (B4), and KIC 2437937 (B5).

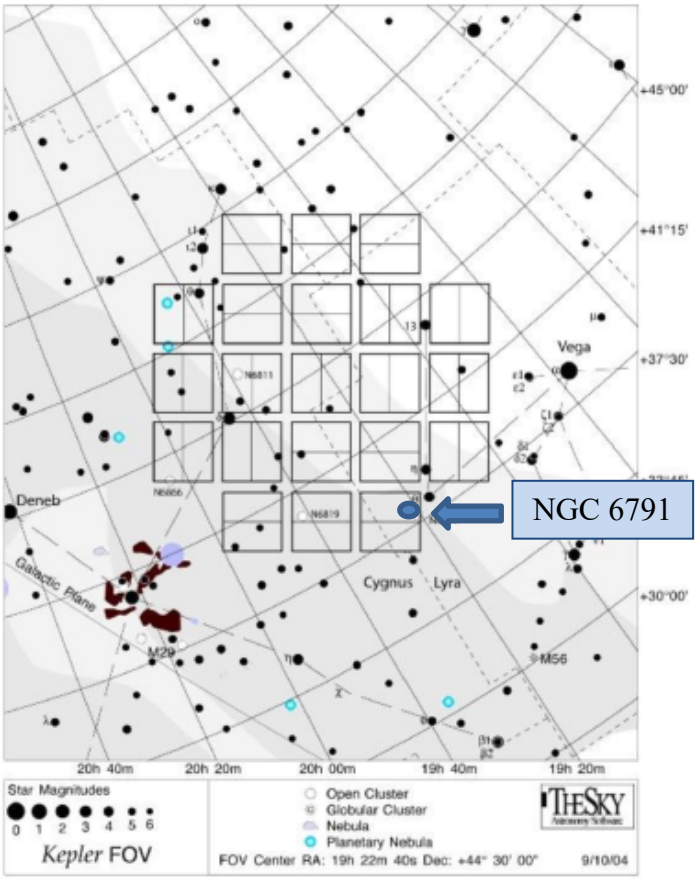

Figure 12: Illustration of *Kepler*'s FOV in the constellations Cygnus and Lyra. Note the position of NGC 6791 as the blue oval in the bottom right corner of the CCD array. *Credit: NASA*

PROPERTIES OF NGC 6791

An Overview of NGC 6791, and the Subdwarf B Stars B3, B4, and B5

NGC 6791 is one of the most metal-rich, oldest open clusters in our galaxy. Recent estimates of the cluster's age and metallicity have confirmed the cluster's old age (7 ± 1 Gyrs; Anthony-Twarog, Twarog, & Mayer, 2007) and high metallicity ([Fe/H] +0.40; Carraro et al., 2006). A photometric study of NGC 6791 (V < 21) was performed by Kałuźny and Udalski (1992) using a 0.9m telescope at Kitt Peak National Observatory (KPNO) which placed a lower mass limit on the cluster of ~4070 $M_{\odot}$. Due to its advanced age, the cluster has a well populated RGB, HB, and lower main sequence. The main sequence turn-off mass has been determined to be 1.15 $M_{\odot}$ (Brogaard et al., 2011), the RGB mass range is 1.03 $M_{\odot}$ to 1.47 $M_{\odot}$ (Basu et al. 2011), and an average red clump (RC) star mass of 1.03 $M_{\odot}$ (Miglio et al. 2012). A recent study by Corsaro et al. (2017) found a preferred stellar rotation inclination between 20° and 30°. They relate this to a transfer of angular momentum from the progenitor molecular cloud.

Kałuźny and Udalski (1992) also reported the discovery of a population of blue objects which were possible hot subdwarfs; labeling them B1 through B8. Four of these (B3, B4, B5, and B6) were confirmed to be sdB stars with effective temperatures ranging from 24,000 K to 32,000 K (Liebert et al., 1994). A follow-up photometric study was done using a 2.1m telescope at KPNO which discovered two new blue stars increasing the total number of hot subdwarfs to ten (Kałuźny & Rucinski, 1995).

A variable star search of NGC 6791 was performed by de Marchi et al. (2007) which confirmed the work of Mochejska, Stanek, Sasselov, and Szentgyorgyi (2002) that

B4 is in a binary system with brightness modulations. Due to the need for high duty cycle, long duration observations, the three sdB stars focused on in this Master's research (B3, B4, and B5) were not discovered to be pulsators until the implementation the *Kepler* space telescope. Of the three sdB stars, B4 was the first to be discovered as a pulsator by Pablo, Kawaler, and Green (2011) who analyzed six months of *Kepler* SC data from quarters 6 (Q06) and Q07. Pablo et al. (2011) was able to perform an asteroseismological analysis of B4's frequency spectrum. They extracted 19 pulsations of which 17 appear to lie on the $l = 1$ asymptotic period sequence (Pablo et al., 2011). Shortly thereafter, Reed, Baran, Østensen, Telting, and O'Toole (2012) discovered B3 and B5 as pulsators from analyzing one month of SC data and three months of LC data from Q11. They extracted 15 total pulsations (11 pulsations from B3 and 4 from B5), and were able to explicitly identify 87% of those with mode identifications of $l = 1$ using asymptotic period spacings (Reed et al., 2012).

An asteroseismic study of 19 RC stars found them to exhibit asymptotic period spacings similar to that of sdB stars in the *Kepler* field (Bossini et al. 2017). The average period spacing for the $l = 1$ sequence in these RC stars was 268.5 ± 0.6 seconds, only slightly larger than that of most *Kepler* sdBs.

Spectroscopy

An atmospheric analyses of B3, B4, and B5 was originally performed by Liebert, Saffer, and Green (1994). They used observations obtained with the 4.5 m Smithsonian-Arizona Multiple Mirror Telescope (MMT). The spectrograph configuration had a 6 Å spectral resolution across optical wavelengths from ~3650 Å to ~5225 Å of B1-B7,

which are shown in Figure 13, as well as two comparison sdO stars, Feige 67 and Feige 110. Focusing on the spectra of our targets only (highlighted in blue in Figure 13), B3, B4, and B5 have very similar spectra, as expected. Most prominent in each spectrum is the Balmer series, whose lines become sequentially weaker at shorter wavelengths. There are also weak helium lines present in the spectra.

Using a range of atmospheric local thermodynamic equilibrium (LTE) models with parameters of 20,000 K < T_{eff} < 40,000 K, 4.0 dex < log g < 6.0 dex, and 0.0 < N[He]/N[H] < 0.1, Liebert et al. (1994) generated synthetic spectra with corresponding step sizes of 5000 K, 0.5 dex, and 0.03 by number. The observed spectra were dereddened prior to analyses with values of E(B-V) = 0.12 and 0.22, and then fitted to the model spectra. The parameters from their fits are given in Table 1.

Table 1: The atmospheric parameters from the fits of the spectra of B3, B4, and B5 with the errors given in parentheses. Column 1 gives the reddening value. Column 2 is the Kałuźny and Udalski (1992) designations. Columns 3-5 give the effective temperatures, surface gravities, and helium abundances. *Credit Liebert et al., 1994*

	Object	**T_{eff}**	**log g**	***y***
E(B-V) = 0.12	B3	24909 (921)	5.55 (0.11)	0.005 (0.002)
	B4	27098 (823)	5.69 (0.10)	0.001 (0.001)
	B5	26332 (1412)	5.59 (0.16)	0.006 (0.003)
E(B-V) = 0.22	B3	24924 (915)	5.56 (0.11)	0.005 (0.002)
	B4	27091 (821)	5.69 (0.10)	0.001 (0.001)
	B5	26360 (1402)	5.60 (0.16)	0.006 (0.003)

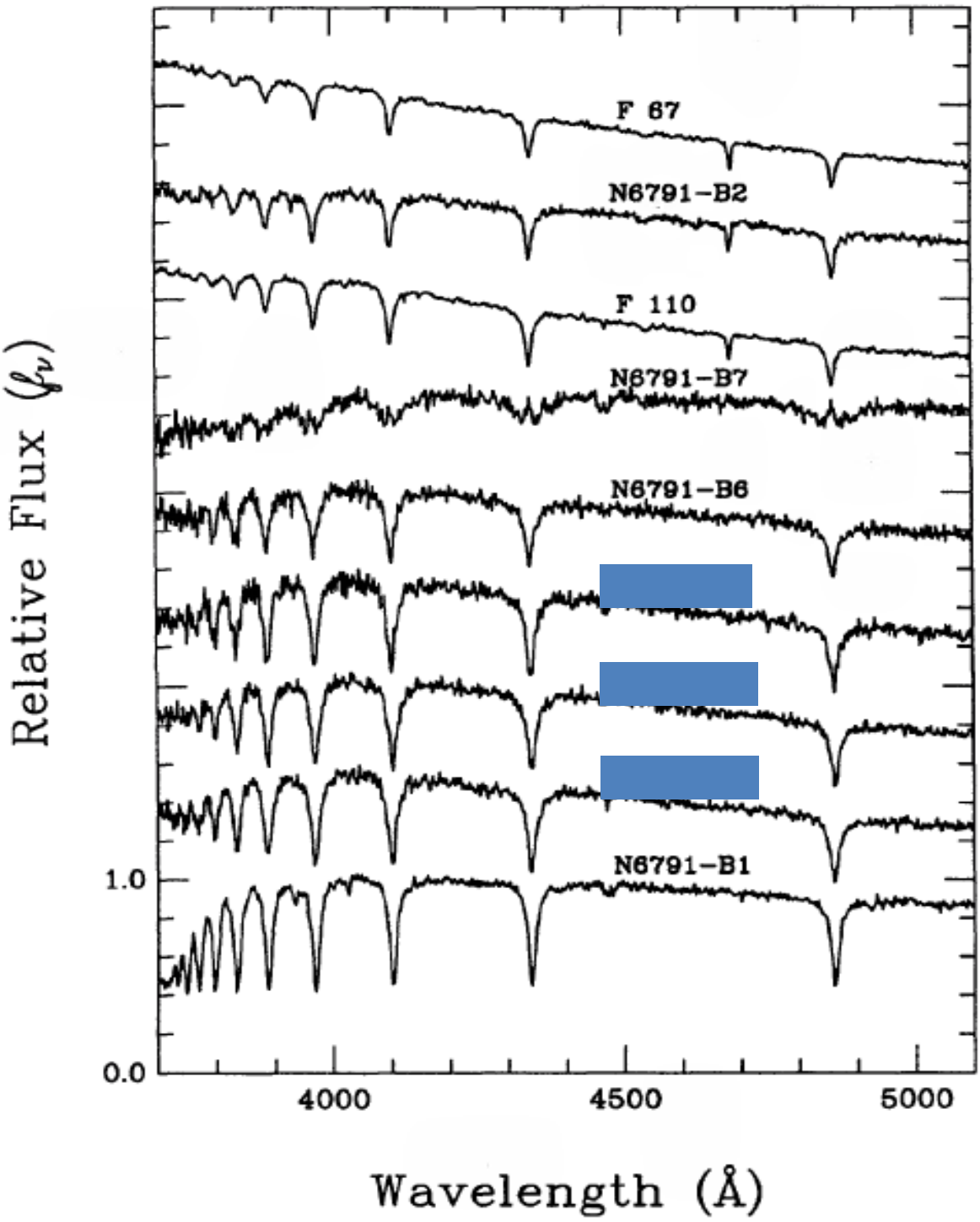

Figure 13: Smithsonian-Arizona Multiple Mirror Telescope spectra of B1-B7 in the open cluster NGC 6791 along with two comparison sdO stars, Feige 67 and Feige 110. From top to bottom, they are ordered by decreasing apparent magnitude where B3, B4, and B5 are highlighted in blue. Note the similarity in B3, B4, B5, and B6. *Credit: Liebert et al., 1994*

Using the atmospheric parameters and assuming values for stellar masses, for which radii were determined, Liebert et al. (1994) calculated the distances to B3, B4, and B5. Three sets of distances were calculated using various distance moduli, reddening values, and stellar masses to show how the variables affect the distance calculations. In all cases, B3, B4, and B5 were affirmed cluster members with average distances of ~ 4 kpc, and the absolute magnitudes of the stars were determined to range from $+4.3 \leq M_v \leq +4.5$ (Liebert et al., 1994).

The angular separation of B3, B4, and B5 are 199", 236", and 123" from the clusters center, outside the ~124" radius where the clusters density goes down by half (Liebert et al., 1994; Kałuźny & Udalski, 1992). Cluster density has been related to binarity (Moni Bidin, Moehler, Piotto, Momany, & Recio-Blanco, 2009). The distance to the cluster has since been determined using various techniques and observations including data from the *Kepler* space telescope (Basu et al., 2011), the Nordic Optical Telescope (NOT; Brogaard et al., 2011), the European Southern Observatory's Very Large Telescope (Brogaard et al., 2011), and the 2 Micron All-Sky Survey (An, Terndrup, Pinsonneault, & Lee, 2015). The distance moduli (distance) values are 13.11 ± 0.06 (4.19 ± 0.12 kpc), 13.51 ± 0.06 (5.18 ± 0.14 kpc), and 13.04 ± 0.08 (4.21 ± 0.15 kpc) for Basu et al. (2011), Brogaard et al. (2011), and An et al. (2015), respectively.

In order to analyze the atmospheric properties of NGC 6791's sdBs using the same techniques and atmospheric models as the other *Kepler* sdB pulsators, spectra from the NOT were obtained using the Andalucía Faint Object Spectrograph and Camera in May 2012 (Reed et al., 2012). The spectra have a resolution of ~ 4 Å across optical wavelengths from 3530 to 5090 Å, and had dispersions of 0.76 Å $pixel^{-1}$. They used the

reduction, fitting techniques, and LTE grid of model atmospheres from Heber, Reid and Warner (2000), and Ramspeck, Heber, and Edelmann (2001) to determine resultant effective temperatures, surface gravities, and helium abundances (Reed et al., 2012); the results are presented in Table 2. From Reed et al. (2012), B3, B4, and B5 have effective temperatures in the range from 23,000 K to 25,000 K; falling well within the g-mode pulsation region on the T_{eff}-log *g* plot (refer to Figure 5). To compare these sibling sdBs with the other known *Kepler* sdBs, I created a T_{eff}-log *g* plot of 35 known pulsating sdBs in the *Kepler* field along with B3, B4, and B5 in Figure 14.

The next chapter describes our processing of the *Kepler* SC and LC data into light curves, and our methodology for determining pulsation frequencies, frequency errors, and amplitudes for our asteroseismic analyses.

Table 2: Columns 1 and 2 are the target designations from Kałużny and Udalski (1992) and the *Kepler* Input Catalog. Column 3 gives the *Kepler* magnitudes. Columns 4, 5, and 6 are the effective temperature, surface gravities, and helium abundances with the errors given in parentheses. *Credit: Reed et al., 2012*

Object	KIC	K_p	T_{eff}	log *g*	$log\ N_{He}/N_H$
B3	2569576	17.801	24250 (459)	5.17 (0.05)	-2.81 (0.12)
B4	2438324	17.924	24786 (665)	5.30 (0.09)	-2.86 (0.20)
B5	2437937	17.978	23844 (676)	5.31 (0.09)	-2.71 (0.22)

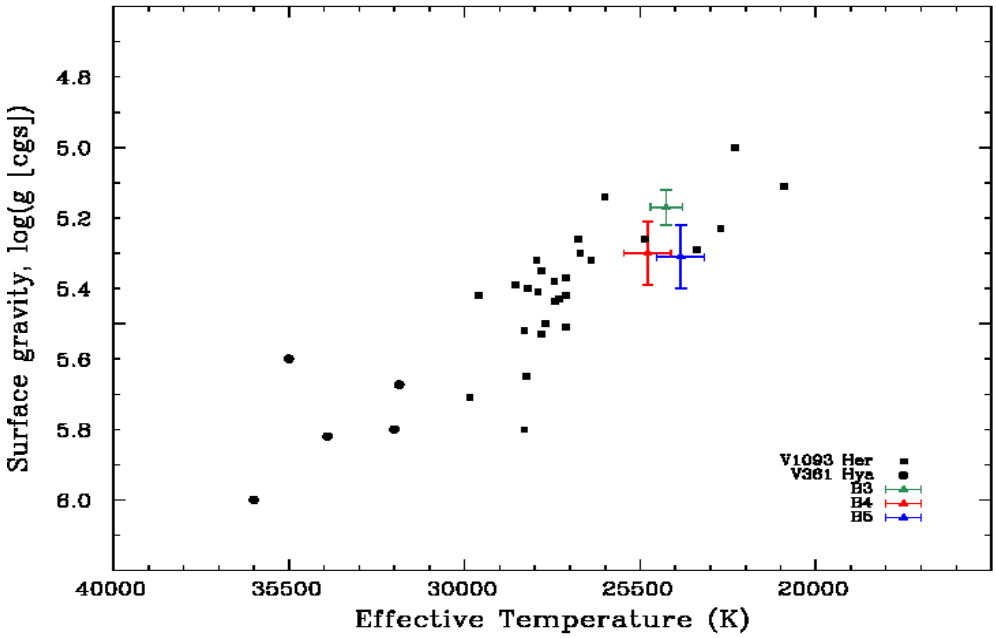

Figure 14: T_{eff}-log *g* plot of known *Kepler* sdB pulsators including B3, B4, and B5. The black circles and squares are p-mode and g-mode pulsating sdB stars, respectively. The green, red, and blue triangles (and their associated error bars) are the NGC 6791 sdB stars B3, B4, B5, respectively.

DATA PROCESSING AND ANALYSES

Short Cadence Data & Long Cadence Data: Super-Aperture Images

I downloaded the *Kepler* short and long cadence data for B3, B4, and B5 from the Mikulski Archive for Space Telescopes (MAST). The data consists of a pixel file (image) for every integration. For B3 and B5, I obtained SC data for Q14 through Q17. For B4, I obtained SC data for Q6 through Q17. Preferably I would have the entire time-domain observed in SC because of the potential for p-mode pulsation frequencies. However, due to the lack of SC data for these targets (especially B3 and B5), I also download the LC data for Q01 through Q17 in an effort to observe the time evolution of the stellar pulsations.

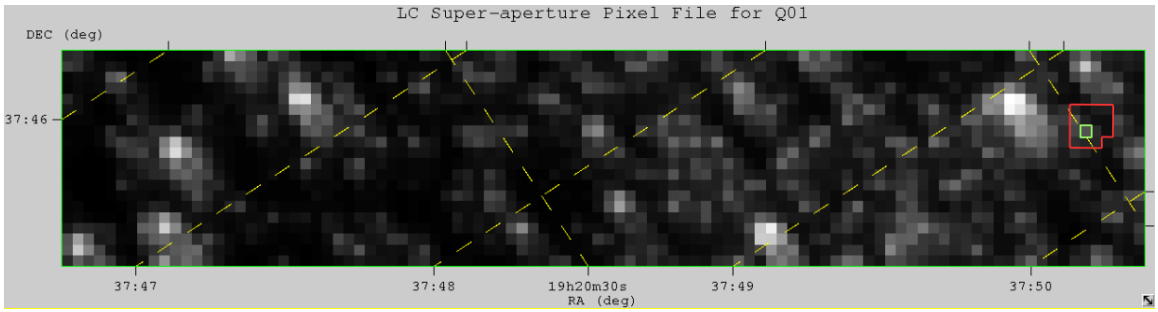

Figure 15: LC super-aperture pixel image of NGC 6791 from Q01 containing B3. The yellow dashed lines indicate the R. A. (downward sloping, left to right) and Dec. (upward sloping). The red outline indicates the pixels searched for optimum extraction, while the green box indicates the pixel containing B3.

The LC data is archived as a super-aperture pixel image 100 x 20 pixels; an example is shown in Figure 15. I extracted fluxes from the super-aperture pixel files to compile the light curves of each star. To determine precisely which pixels our target falls

on, I searched a 3 x 3 grid of pixels surrounding the listed R. A. and Dec. of our targets as designated from MAST. Since *Kepler* data are regularly sampled and it is known that our targets are pulsators, I extracted the fluxes from each pixel individually and took their Fourier transforms (FTs) in order to locate the pixels which have the highest amplitude pulsations. If these lie on the edge of our grid, I again searched a 3 x 3 grid (or larger) but centered on the pixel with the highest amplitude pulsations. The FTs of the 15 pixels used in the grid searches for B3 are shown in Figure 16.

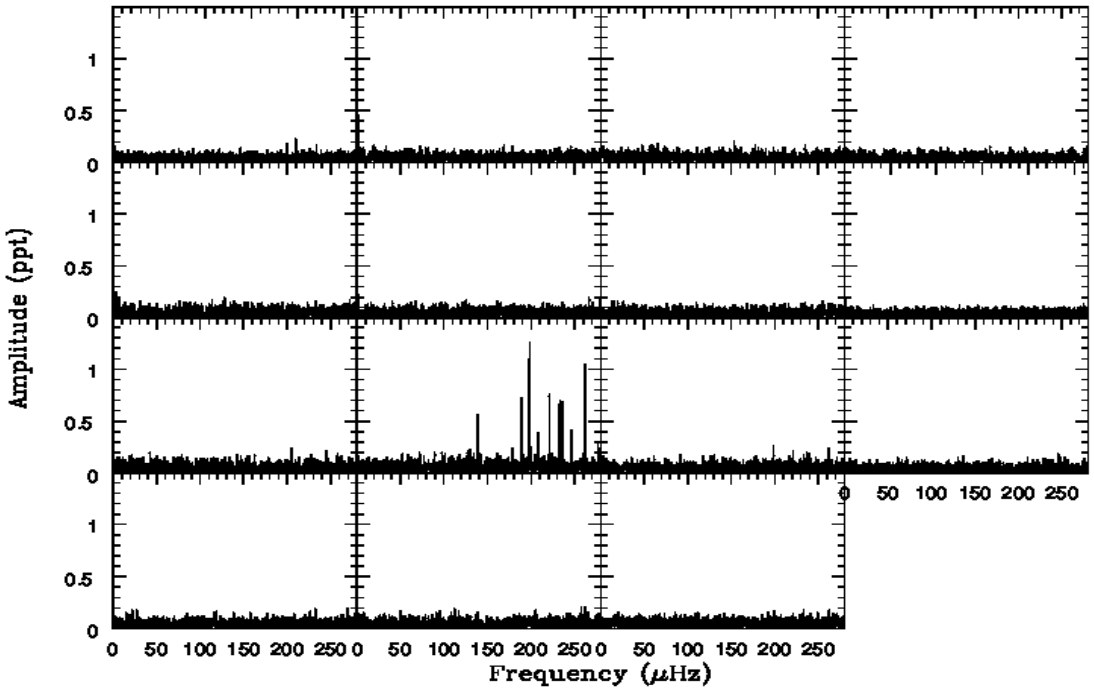

Figure 16: The FTs of the 15 pixels (outlined in red from Figure 15) used in the search for B3. Note the obvious pulsations in pixel 2, 2 which corresponds to physical pixel 95, 13 (outlined in green from Figure 15).

Using the pixels which contain signal from our targets, I created pixel masks of all the possible pixel combinations and took their FTs in order to determine which exhibit

the highest pulsation amplitudes, thus defining the optimum pixel mask. After determining the optimum pixel mask for rotation one, I repeated the process for the other three spacecraft rotations. This is necessary because, while CCD array is rotationally symmetric, the optical distortions and pixel sensitivity vary for the different orientations. I applied the masks for each rotation to the corresponding quarters of data (i.e. rotation one corresponds to Q01, Q05, Q09, Q13, and Q17, while rotation two corresponds to Q02, Q06, Q10, and Q14, etc.), and I extracted the LC fluxes from Q01 through Q13 for B3. I then repeated the entire process from grid searching to optimum LC light curve extraction for B4 from Q01 through Q05 and B5 from Q01 through Q13.

All three stars were guest observer targets during the course of the K1 mission, which means the SC target pixel files for all three stars have been archived and selected out of the broader cluster field; an example is given in Figure 17. I processed the SC pixel files in the same way as I did the LC data. Briefly, I tested a large area of pixels surrounding the R. A. and Dec. of the targets in order to pinpoint which pixels contain pulsation data. I tested all possible combinations of pixels in order to optimize the final pixel mask. The optimum pixel mask for each rotation of the spacecraft was applied to their corresponding quarters. Finally, the fluxes from the SC data of B3 and B5 in Q14 through Q17 were extracted as well as Q06 through Q17 for B4.

Light Curves

After extracting the fluxes from the available data, I combined the SC and LC data into a single light curve for each star that spans the entire 17 quarters of observation; shown in Figure 18.

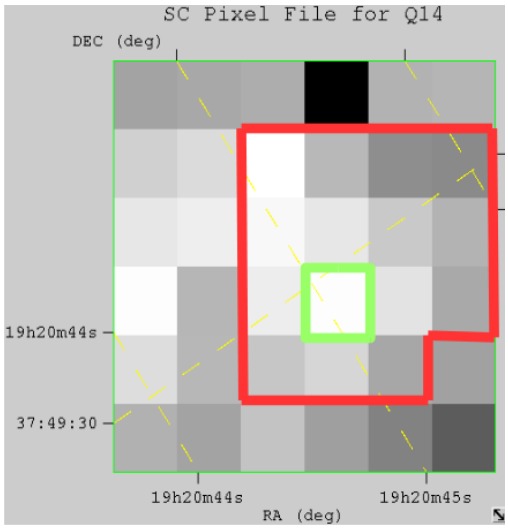

Figure 17: SC target pixel image for B3 in Q14. The green outlined pixel contains the position of B3. The red outline indicates the pixels searched during the LC data processing (see Figure 15).

Since with each rotation, the stars fall on different CCDs with different sensitivities, this creates variations in signal and noise, which offset each subset of data. I removed long-term trends using ancillary data which models the systematic trends in flux (*Kepler* basis vectors), and spline fit each quarter of data. Since the pulsation analyses are dependent upon deviations from the average, I scaled the normalized amplitudes of each quarter and removed data points exceeding a 5-sigma deviation from the average in order to eliminate superfluous data points and prevent artifacts from appearing in the FTs. In total, I accrued ~460,000 observations each for B3 and B5, and ~1.44 million observations for B4. These span ~1,460 days with a duty cycle of 82.9%, 84.4%, and 83.9% for B3, B4, and B5, respectively.

Fourier Transform and Pulsation Frequencies

In order to determine pulsation frequencies, I created FTs of the discrete light

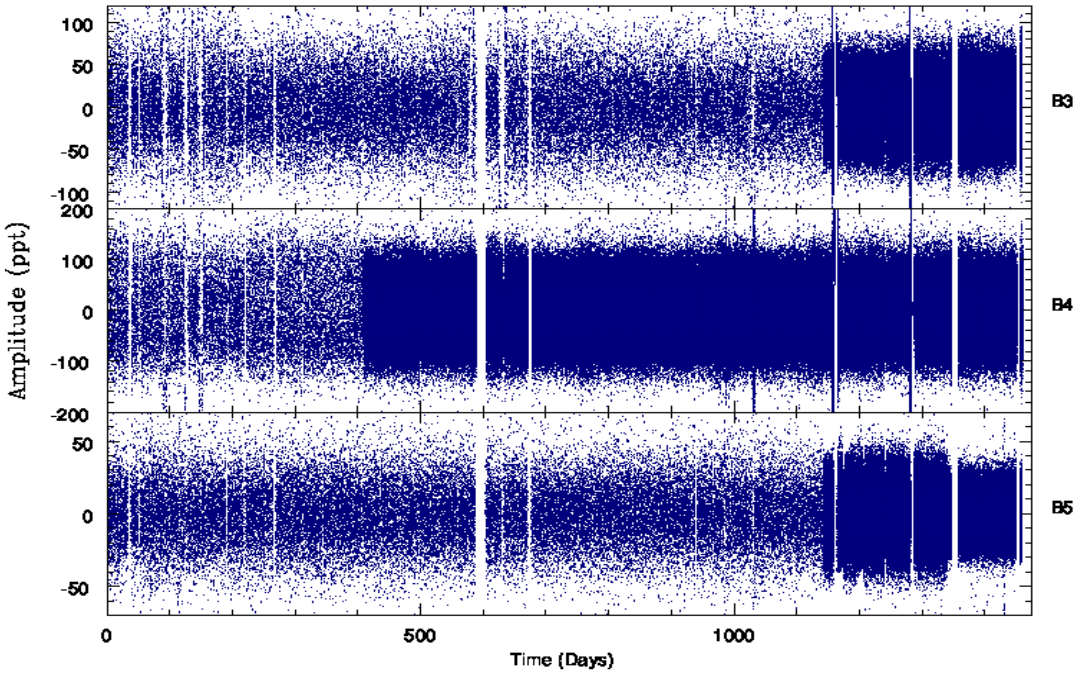

Figure 18: The light curves of B3 (top panel), B4 (middle panel), and B5 (bottom panel). Notice the transition from LC to SC data for B3 and B5 at ~1,150 days whereas for B4 the transition is at ~400 days.

curves presented in Figure 19. Due to the combination of SC and LC data, the FTs of each star have two Nyquist frequencies, one for each cadence. I use a 1.5/T temporal resolution which is 0.012 μHz for the entire data set of all three stars. This temporal resolution and the combination Nyquist frequency LC and SC data of each star (7431 μHz for B3, 7782 μHz for B4, and 7463 μHz for B5) allows us to determine false-alarm probabilities for peak detection in the FTs using a normal Gaussian distribution and the probability density function. I calculate significance levels of 0.99999841, 0.9999979, and 0.99999841 for B3, B4, and B5, respectively, which require detection thresholds of 4.8σ (B3), 4.7σ (B4), and 4.8σ (B5). I calculate these to be 0.332 ppt (B3), 0.291 ppt (B4), and 0.186 ppt (B5), respectively (Bevington & Robinson 2003). For smaller subsets

of data, the detection thresholds were calculated accordingly. The FTs of the entire data set of B3, B4, and B5 are plotted in Figure 19 up to 1250 μHz corresponding to three reflections about the LC Nyquist (~283 μHz for all three stars) and its overtones.

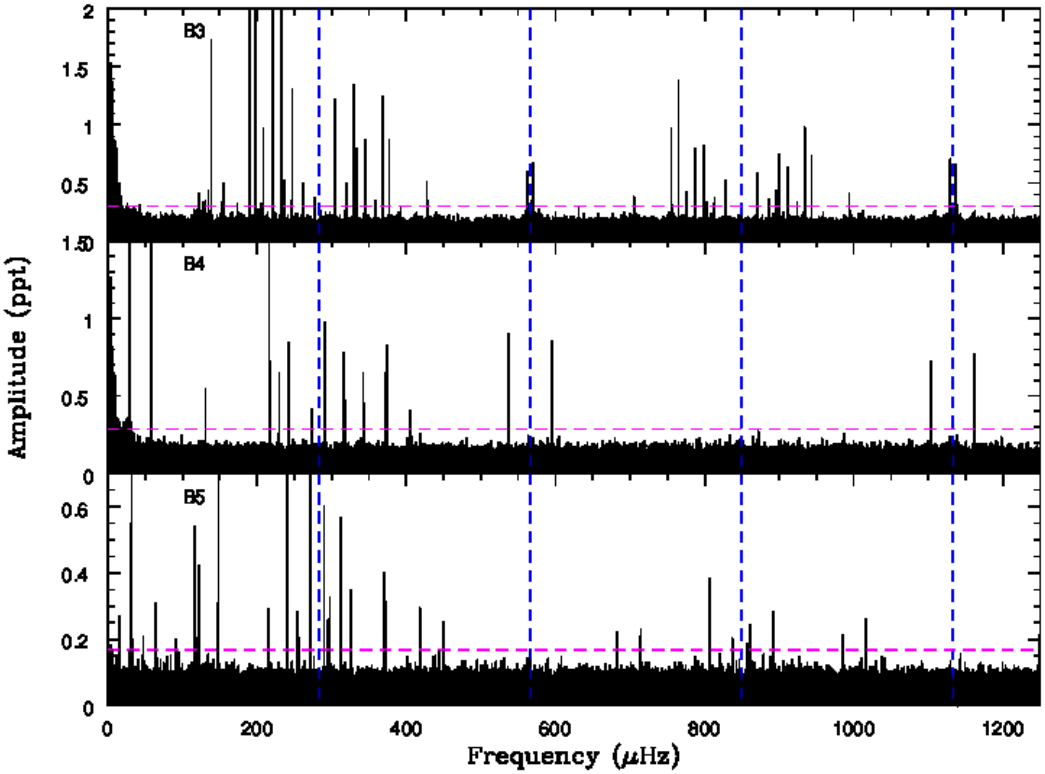

Figure 19: The FTs of B3 (top panel), B4 (middle panel), and B5 (bottom panel) plotted to 1250 μHz. Notice the g-mode pulsations between 0 and ~280 μHz, and their reflections about the three LC Nyquist overtones (denoted by the blue dashed lines). The magenta dashed line represents the detection thresholds of each star.

I examined the time evolution of the stellar pulsations for B3, B4, and B5 by creating sliding Fourier transforms (SFTs). I create SFTs by first generating a single FT using a subset of data of a specified length starting at day zero. Since the longest rotation periods of *Kepler* sdB stars is roughly 100 days, I choose FTs of 200 day length in order to resolve the potential frequency multiplets of B3 and B5. I then step the process

forward by five days and create another 200 day long FT. I repeat this over the entirety of the ~1,400 days of observations in order to stack all of the FTs into one final plot with frequency plotted on the x-axis, time on the y-axis, and the amplitude of the pulsations represented by the color scale; an example of a SFT for B3 is given in Figure 20.

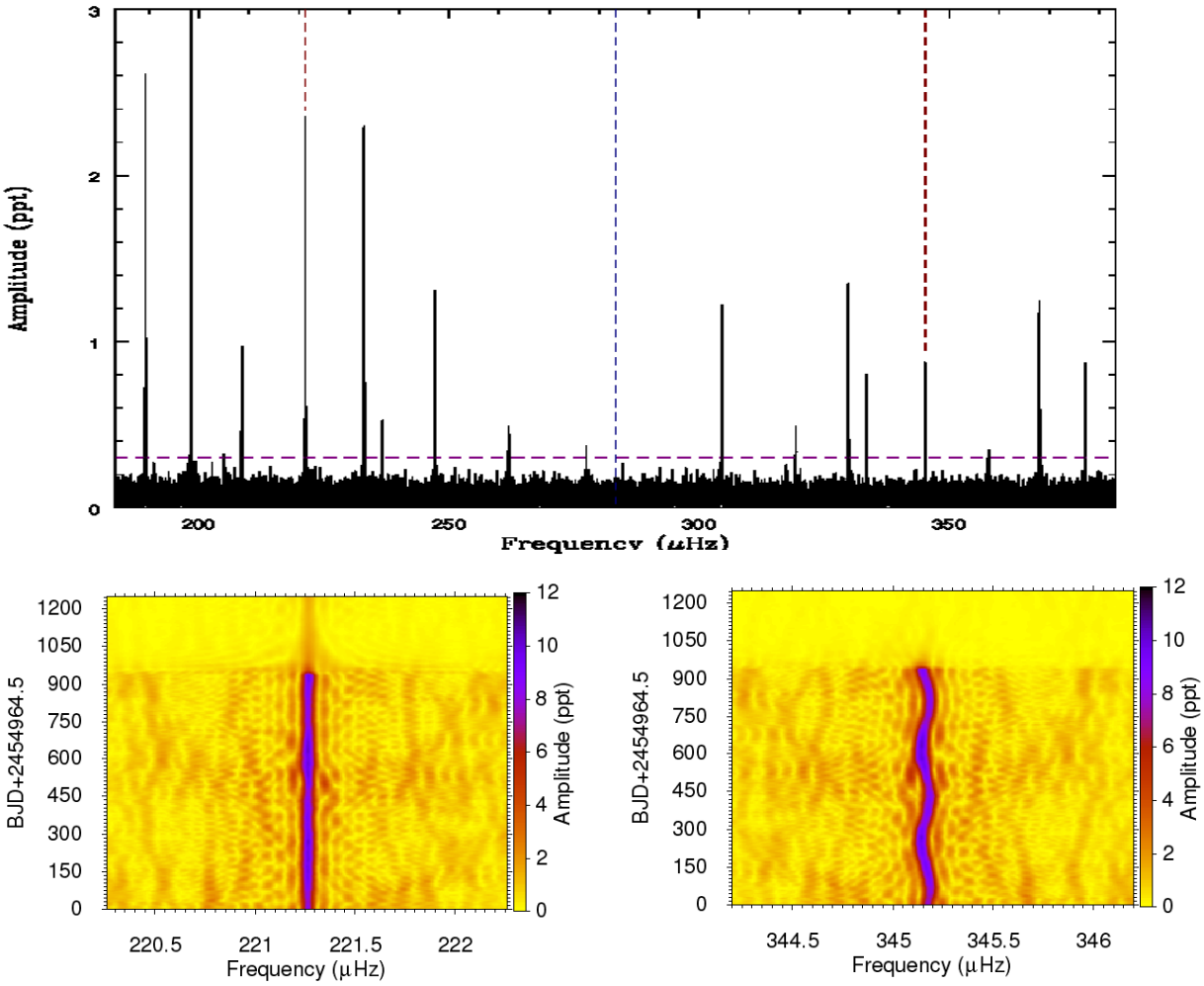

Figure 20: *Top panel;* FT of B3's frequency spectrum near the LC Nyquist frequency at 283.25 μHz indicated by the blue dashed line. The red dashed lines correspond to an intrinsic pulsation (left) and its Nyquist reflection (right), while the magenta line indicates the detection threshold. *Bottom panels;* SFTs depicting the time evolution of the intrinsic pulsation at 221.2643 μHz (left) and its reflection at ~345 μHz (right). Notice the sinusoidal behavior of the reflection throughout observations as well as its non-detection in the SFT when BJD+2454964.5 > 965 days due to the transition to SC data only. The amplitudes in the SFTs are given in ppt in order to compare with the amplitudes in the overall FT in the top panel.

An oddity with having multiple cadences within a larger data set is the effect of multiple Nyquist reflection points (refer to Figure 19). Between the LC Nyquist and the SC Nyquist, pulsations can be reflected over 30 times which makes detecting pulsations past the first LC reflection difficult. While the LC data creates reflections throughout the frequency spectrum, these LC reflection amplitudes go to zero in the temporal spectrum of the SFT where the subsets are purely SC data as shown for days greater than 965 in the bottom-right panel of Figure 20. However, if a pulsation is a LC Nyquist reflection, then the pulsation varies much more in frequency and amplitude than the intrinsic counterpart; an example for B3 is given in the bottom panel of Figure 20. Therefore, exploitation of the SC data in the SFTs can also be used to determine which pulsations are intrinsic to the star.

Pulsations which are intrinsic to the star are extracted from the FT in one of two ways; prewhitening or Lorentzian fitting. Prewhitening is fitting a sinusoidal wave to the light curve and removing it, which should also remove the peak in the FT. Lorentzian fitting is just that, fitting a Lorentzian to the pulsation's profile in the FT. If the amplitude of any pulsation is nearly constant throughout the entirety of observations, then I prewhiten the frequency. For the frequency at 198.4234 μHz (shown in Figure 21), the prewhitening technique reduced the peak to ~10% of its original amplitude which is nearly equal to our detection threshold. By extracting the pulsation to an amplitude very close to our detection threshold, this ensures that the entire pulsation has been removed including its reflected counterparts. This prewhitening result is indicative of the results for all prewhitened peaks, and determines the frequency and amplitude to a greater level of precision than Lorentzian fitting. If prewhitening fails, then the pulsation is fit using a

Lorentzian profile from which the full-width half-maximum is used as an estimate of the error in frequency. Using the prewhitening technique or Lorentzian fitting, I extracted a total of 30 pulsations for B3, 20 for B4, and 17 for B5. These pulsations are all driven in the g-mode region ($\leq$ ~400 μHz) with only three potential *p* modes detected in B3, which themselves are very close to the detection threshold.

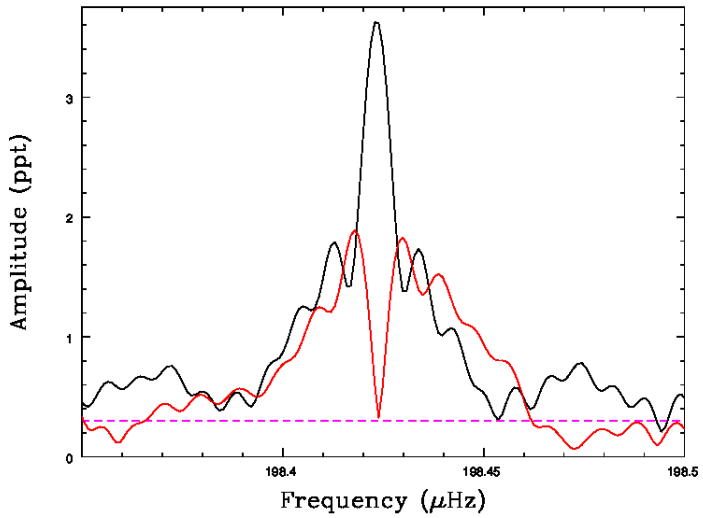

Figure 21: The prewhitened frequency at 198.4234 μHz is shown in red with the original frequency peak plotted in black. The detection threshold is the dashed magenta line.

The next chapters will present the results of our analyses of the entire *Kepler* data sets for B3, B4, and B5 from which I build on the asteroseismological results of Pablo et al. (2011) and Reed et al. (2012). I will analyze B3, B4, and B5's pulsations using the tools of asteroseismology in order to identify pulsation modes, and compare the similarities or differences in asymptotic period spacing values, frequency splittings, and other asteroseismic parameters. I will then discuss results and their insight into the internal structure and evolution of these stars.

ASTEROSEISMIC ANALYSES

Using the entire *Kepler* data set, I extracted a total of 67 pulsations from B3, B4, and B5, expanding the list of known pulsations for these stars by ~200%. In the following sections, I present the detailed asteroseismic analyses of each star's pulsations, including the discovery of rotationally induced frequency splittings and the confirmation of asymptotic g-mode period sequences.

B3: KIC 2569576

For B3, I was able to expand the known pulsation list by 21 frequencies in addition to the recovery of all but two pulsations detected by Reed et al. (2012). Of the two pulsations that were not recovered from Reed et al. (2012), one was labeled tentative in their list due to its low S/N, which, in the full data set, did not exceed our detection threshold. The other, which was observed only in the LC data in the Reed et al. (2012) analysis, was the LC Nyquist reflection of the pulsation at 329.852 μHz. Therefore I excluded both f3 and f11 (as denoted in Reed et al., 2012) from our final list.

Rotationally Induced Frequency Multiplets. From the analysis performed by Reed et al. (2012) on four months of B3 data, no frequency splittings were found for B3. Using the entire *Kepler* data set, I searched for rotationally induced frequency multiplets and detected nine frequency splittings of ~0.090 μHz and one splitting roughly twice that, all in the g-mode region. These splittings are found in the majority of the highest amplitude pulsations, so, with the knowledge of geometric cancellation effects (Pesnell 1985), I expect these splittings to be attributed to $l = 1$ pulsation modes and tentatively

identify them as such. While five of B3's splittings appear as doublets (with all but one interpreted as $\Delta m = 1$), two multiplets resolve as triplets; an example of which is shown in Figure 22. The average amplitudes of all of B3's multiplets, each normalized to the $m = 0$ component, is shown in Figure 23. In total, 17 $l = 1$ pulsations were detected with an average frequency splitting of 0.090 ± 0.013 μHz.

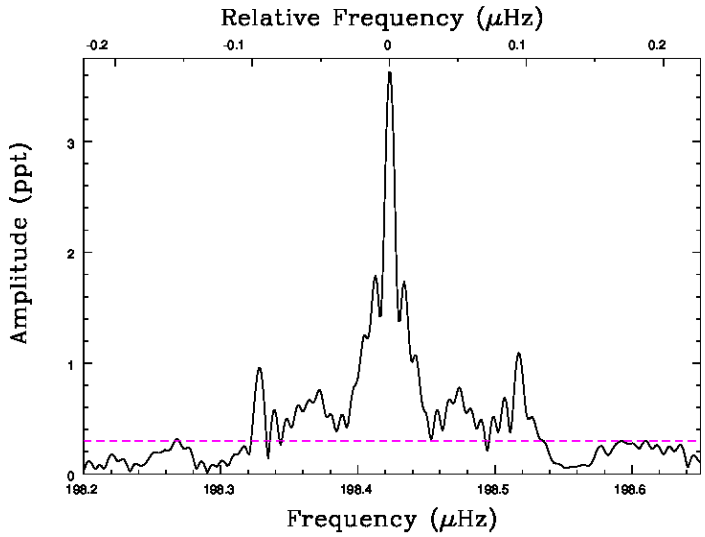

Figure 22: The frequency multiplet of B3 at 198.4234 μHz. The dashed magenta line is the detection threshold. Note the splittings of ~0.090 μHz.

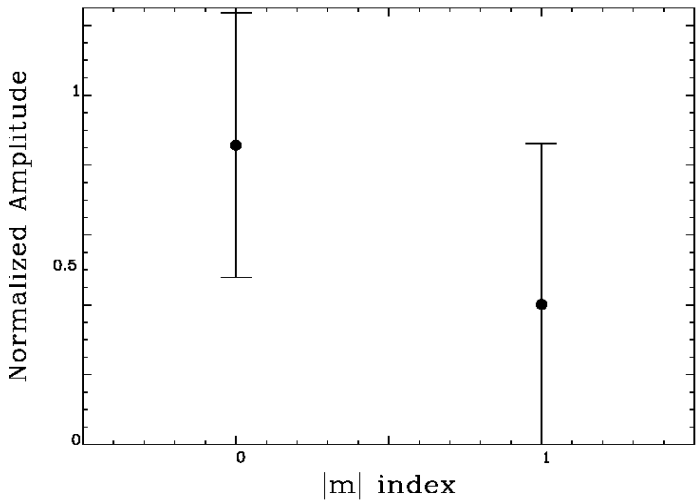

Figure 23: The average normalized amplitudes for the azimuthal components of the $l = 1$ frequency splittings of B3 and their associated error bars.

Asymptotic Period Spacings. Asymptotic period spacings in the *g* modes of pulsating sdB stars is a phenomenon that has become a well-established indicator of pulsation modes, where $l = 1$ and 2 modes have spacings of roughly 250 and 145 seconds (Reed et al., 2011). Our method for determining mode identifications via period spacing relationships begins by determining the period spacing values present in our list using the KS test. The confidence intervals for this test were calculated from the KS-Test results of 1000 random lists of periods on the same magnitude and range as the target list. The calculated KS test statistics for B3 and their confidence intervals are presented in Figure 24. There are three troughs which eclipse the 99.9% confidence level. Most notably, the largest trough at ~250 seconds indicating a strong $l = 1$ sequence. The second deepest trough at ~125 seconds (250 seconds divided by two) and the third deepest trough at ~80 seconds (roughly 250 seconds divided by three) are both overtones of the $l = 1$ sequence.

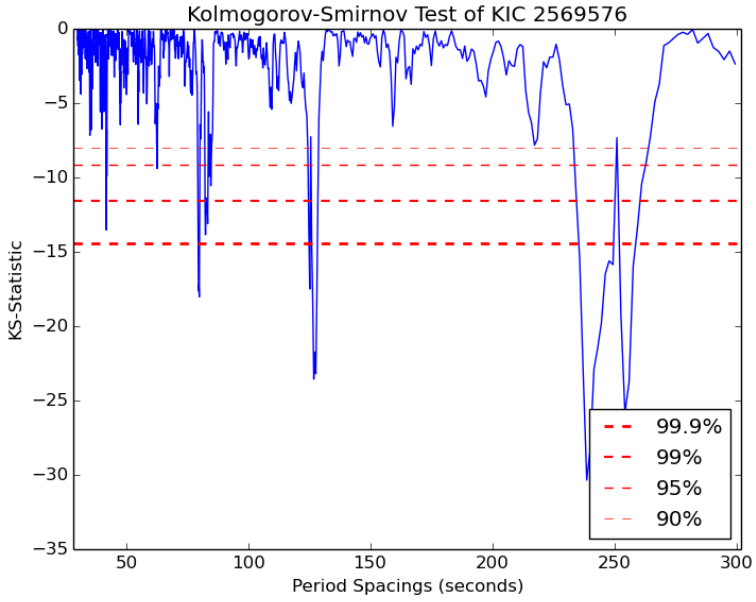

Figure 24: The KS test for B3 plotted with confidence intervals given in the legend. Note the large KS statistics for $l = 1$ period spacings at ~250 seconds and its overtones at ~125 and ~80 seconds.

To determine which pulsations fall on sequences, I produced échelle diagrams folded over the period selected from the KS test. Periods which aligned vertically on the échelle diagram were selected as sequence member. I performed a linear regression of the pulsation periods and their tentative overtones. Similar to all other asteroseismic analyses of *Kepler* sdB stars, only pulsations that fell within 10% of the fit were identified as members of the sequence, which I consider a reasonable error. These were subsequently added to the sequence and used to update the fit.

In B3, I was able to identify a total of 20 pulsations which lie on the $l = 1$ sequence with an average spacing of 252.27 ± 0.66 seconds. Using the observed $l = 1$ sequence, I calculated the $l = 2$ sequence using the explicit relationship between the $l = 1$ and 2 sequences given by equation three on page 14. Four pulsations were found to lie on the $l = 2$ sequence, however, two of these overlap with the $l = 1$ sequence.

From these I determined an average period spacing for the $l = 2$ sequence of 145.55 ± 0.25 seconds. To confirm these sequences I calculated the period modulo for each sequence and visually inspected the échelle diagrams of both spacings which are shown in Figure 25. No obvious sequence is observed for the $l = 2$ period modulo. However, there is a nearly continuous sequence from $n = 8$ to 17 (only missing members $n = 10$ and 11) in the $l = 1$ period sequence. The échelle diagram is unremarkable in features such that the sequence shows no meaningful deviations. In total, I was able to identify 73% of B3's pulsations as $l = 1$ and/or 2 using asymptotic period spacings.

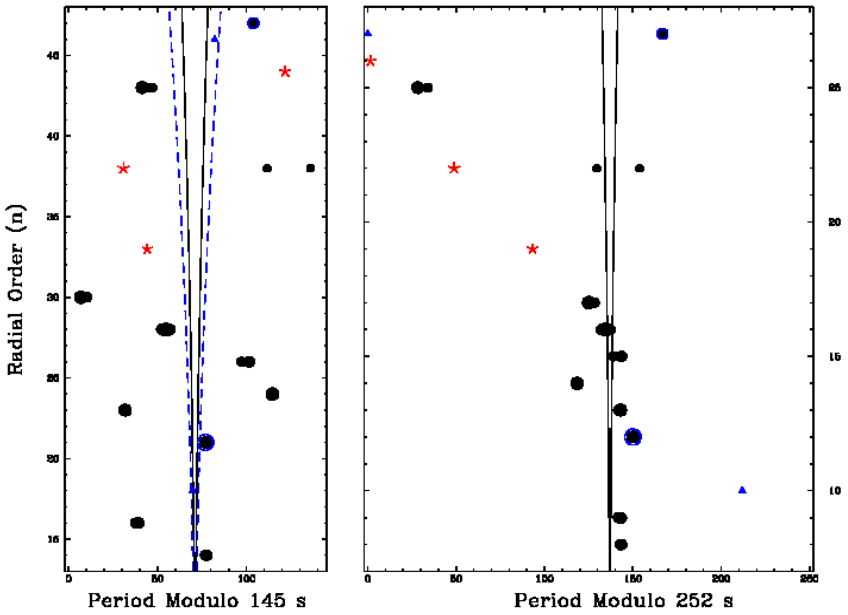

Figure 25: The echelle diagrams of B3 for the l = 1 g-mode pulsation sequence (right panel) and the l = 2 (left panel). The black dots are identified as l = 1, blue triangles are l = 2, black dots with blue circles are l = 1 and 2, and red asterisks are unknown. The solid lines indicate the calculated position of the m = ±1 components based on the frequency splitting of B3. The dashed lines correspond to the m = ±2 components.

Mode Identification. In summary, I used rotationally induced frequency splittings and asymptotic period spacings to identify pulsation modes for 80% of the total pulsations of B3. B3 has ten multiplets, one of which does not fit the asymptotic period sequence. Therefore, 15 of the 24 identified modes are corroborated with evidence from both mode identification methods; the results are presented in Table 3. There are also three p modes detected. The predicted overtone spacing of p modes is roughly 1000 μHz. Pulsations f28 and f29 are spaced by ~1300 μHz, while f29 and f30 are spaced by ~1800 μHz (twice 900 μHz), which are approximately the predicted overtone spacing.

Table 3: Pulsation frequencies of B3. Italicized frequencies were prewhitened. The first three columns give the pulsation ID's, frequency, and period with the errors given in parentheses. Columns 4 and 5 are the pulsation amplitudes in relation to detection thresholds (S/N) and in ppt. Columns 6 and 7 give the ratio (in percent) of the change in period to the period spacing for a given degree *l* to denote the deviations from asymptotic model sequences. Columns 8-10 give the mode identifications from our results. Column 11 gives the frequency splittings.

ID	Frequency μHz	Period Seconds	S/N	Amplitude ppt	$\Delta P/\Delta\Pi_{l=1}$ %	$\Delta P/\Delta\Pi_{l=2}$ %	*l*	*m*	*n*	Δν μHz
f1	127.489 (0.017)	7843.81 (1.06)	4.67	0.323	8.9	4.9	1, 2	-	27, 47	
f2	130.258 (0.024)	7677.07 (1.42)	4.75	0.328		-9.7	2	-	46	
f3	134.650 (0.020)	7426.66 (1.10)	6.23	0.430						
f4	138.754 (0.010)	7207.00 (0.51)	8.68	0.600			1	-1		0.108
f5	138.862 (0.015)	7201.39 (0.77)	27.95	1.930			1	0		
f6	152.187 (0.017)	6570.86 (0.75)	4.77	0.330	4.3		1	-	22	
f7	152.751 (0.010)	6546.60 (0.44)	4.77	0.329	-5.4		1	-	22	
f8	*154.6579 (0.0009)*	*6465.884 (0.038)*	7.24	0.500						
f9	173.784 (0.013)	5754.27 (0.43)	4.60	0.318						
f10	*189.2074 (0.0006)*	*5285.207 (0.017)*	11.82	0.817	-5.4		1	-1	17	0.114
f11	*189.3214 (0.0009)*	*5282.023 (0.025)*	39.11	2.701	-6.7		1	0	17	
f12	*198.3320 (0.0008)*	*5042.051 (0.020)*	13.29	0.918	-1.8		1	-1	16	0.091
f13	*198.4234 (0.0001)*	*5039.728 (0.003)*	52.14	3.601	-2.7		1	0	16	0.093
f14	198.516 (0.016)	5037.38 (0.40)	14.73	1.017	-3.6		1	1	16	
f15	*208.4836 (0.0005)*	*4796.540 (0.011)*	14.61	1.009	0.9		1	-1	15	0.189
f16	*208.6725 (0.0008)*	*4792.198 (0.019)*	8.69	0.600	-0.8		1	1	15	
f17	*221.2643 (0.0002)*	*4519.482 (0.004)*	38.56	2.663	-9.0		1	-	14	
f18	*232.9928 (0.0002)*	*4291.978 (0.004)*	31.63	2.185	0.9		1	0	13	0.069
f19	*233.0613 (0.0008)*	*4290.717 (0.014)*	9.22	0.637	0.4		1	1	13	
f20	*247.0965 (0.0003)*	*4047.002 (0.004)*	26.66	1.841	3.9	-1.9	1, 2		12, 21	
f21	277.403 (0.013)	3604.86 (0.17)	5.47	0.378		-5.5	2		18	
f22	304.463 (0.011)	3284.47 (0.12)	14.60	1.008	1.6		1	-1	9	0.079
f23	304.542 (0.008)	3283.62 (0.08)	16.33	1.128	1.2		1	0	9	0.082
f24	304.624 (0.011)	3282.74 (0.11)	12.33	0.852	0.9		1	1	9	
f25	329.690 (0.007)	3033.15 (0.07)	7.96	0.550	2.0		1	-1	8	0.084
f26	329.774 (0.010)	3032.38 (0.09)	17.95	1.240	1.7		1	0	8	0.078
f27	329.852 (0.015)	3031.66 (0.14)	8.62	0.595	1.4		1	1	8	
f28	2819.950 (0.005)	354.616 (0.001)	4.65	0.321						
f29	4148.320 (0.009)	241.061 (0.001)	4.51	0.311						
f30	5968.536 (0.003)	167.5452 (0.0001)	4.55	0.314						

B4: KIC 2438324

For B4, I was able to recover 84% of the pulsations detected by Pablo et al. (2011) on top of which I detected two additional frequencies. The three pulsations that were not recovered from Pablo et al. (2011) were all low amplitude, and two of them they listed as tentative. All were observed at low amplitudes in early quarters, however, the pulsations are not observed in later quarters and do not rise above our detection threshold for the entire data set, so I do not include them in our final list.

Rotationally Induced Frequency Multiplets. Previously, Pablo et al. (2011) observed $l = 1$ multiplets with $\Delta m = 1$ frequency splittings of 0.620 μHz in B4's frequency spectrum. Using the entire *Kepler* data set of each star, I detected two frequency splittings of 0.611 and 0.596 μHz in a triplet and five with splittings roughly twice that in doublets. These splittings were observed in 75% of the highest amplitude pulsations, so similar to B3, I expect these splittings to be attributed to $l = 1$ pulsation modes. Given this, B4's triplets have splittings that are $\Delta m = 2$. An example of the $l = 1$ triplet is shown in Figure 26 with the average normalized amplitudes of all of B4's multiplets shown in Figure 27. In total, 13 $l = 1$ pulsations were detected with an average frequency splitting of 0.629 ± 0.012 μHz.

Asymptotic Period Spacings. I determined the period sequences of B4 in the same manner as described for B3. Of all three sdB stars analyzed in this research, B4 has the strongest $l = 1$ sequence; the $l = 1$ trough at ~240 seconds in the KS test of B4's pulsations is shown in Figure 28. Aside from the orbital frequency (29.0441 μHz) and its overtone (58.0894 μHz), the $l = 1$ period sequence encompasses 100% of the extracted pulsations. The average spacing from these 18 $l = 1$ pulsations is 236.2 ± 2.1 seconds.

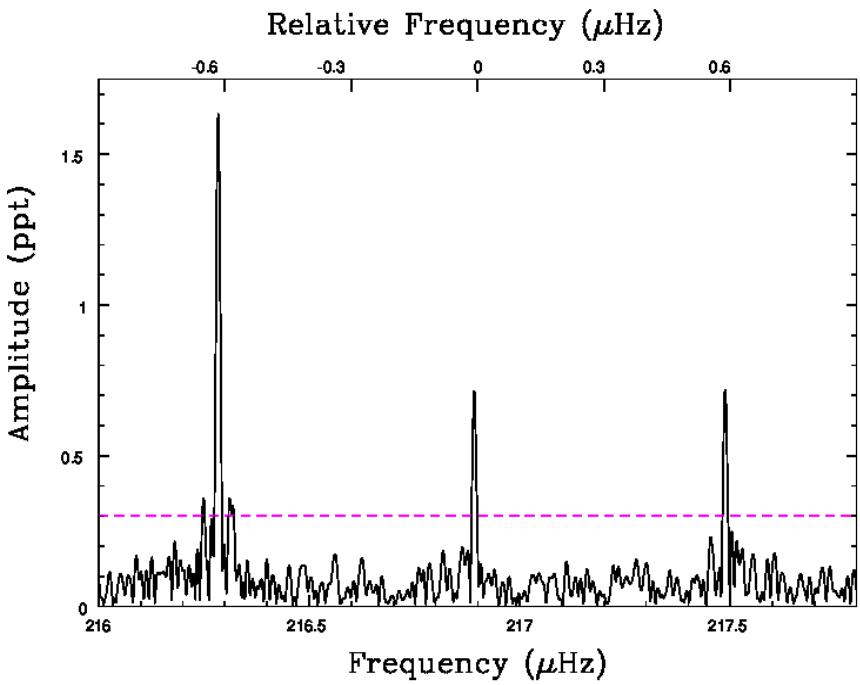

Figure 26: The plot of a frequency multiplet of B4 at 216.893 μHz with frequency splittings of 0.611 (left splitting) and 0.596 μHz (right splitting). The dashed magenta line is the detection threshold.

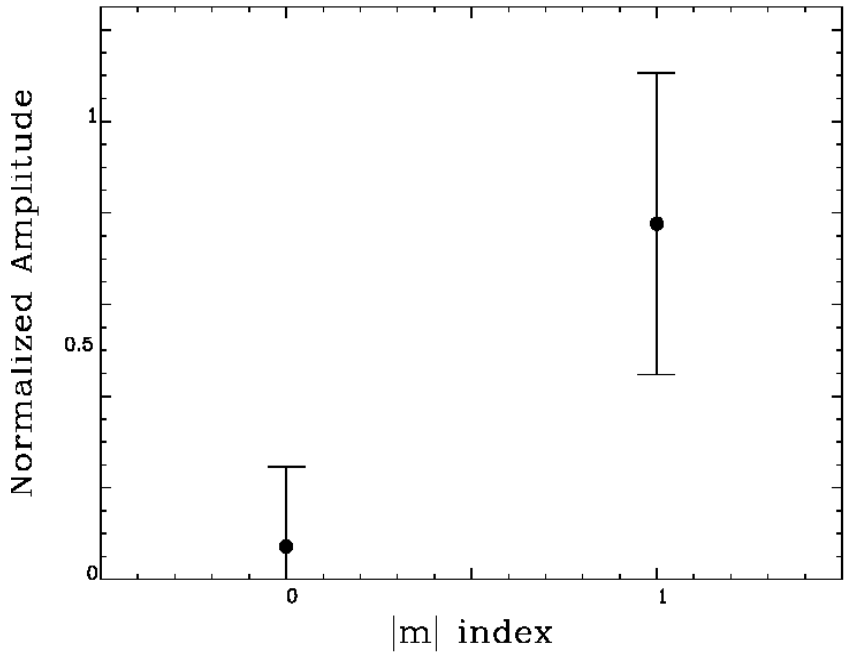

Figure 27: The average, normalized amplitudes for the azimuthal components of the $l = 1$ frequency splittings of B4 and their associated error bars.

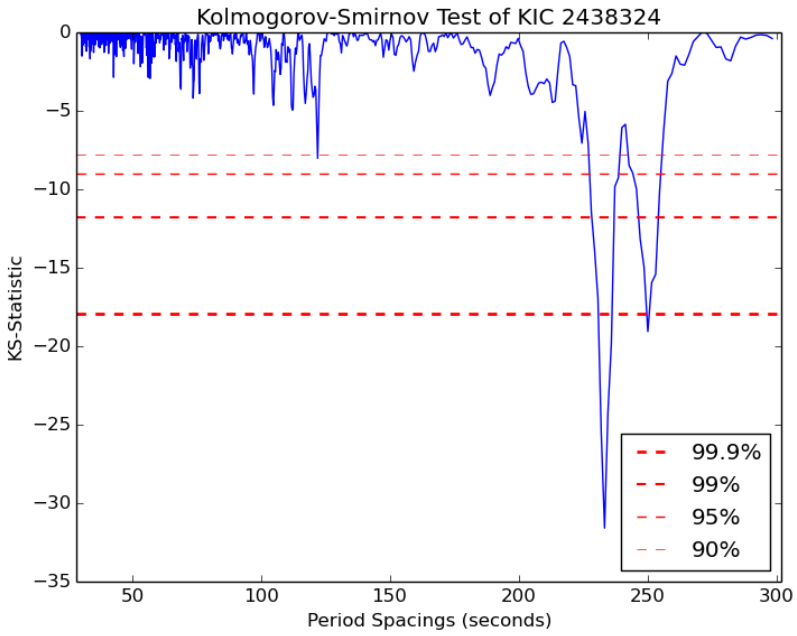

Figure 28: The KS test for B4 plotted with confidence intervals as given in the legend. Note the KS statistic for the l = 1 period spacings at ~240 seconds.

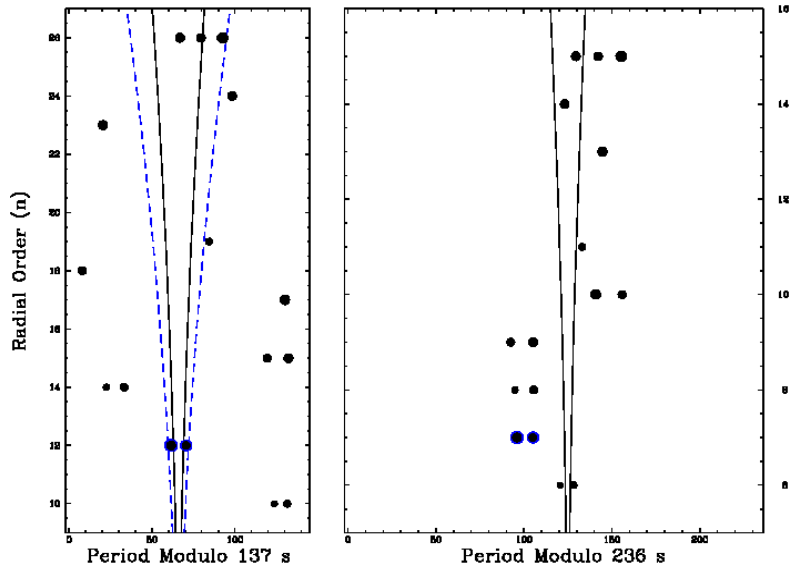

Figure 29: The echelle diagrams of B4 for the l = 1 g-mode pulsation sequence in the right panel, and the l = 2 sequence in the left panel. The black dots are identified as l = 1, blue triangles are l = 2, black dots with blue circles are l = 1 and 2, and red asterisks are unknown. The solid lines indicate the calculated position of the m = ±1 components based on the frequency splitting of B4. The dashed lines correspond to the m = ±2 components.

Using these, I calculated the $l = 2$ sequence on which only three pulsations were found to lie, all overlap with the $l = 1$ sequence. The échelle diagrams of both sequences is shown in Figure 29. One of the three potential $l = 2$ pulsations is part of an identified $l = 1$ triplet. Only the two pulsations (f17 and f18) remain potential $l = 2$ pulsation modes. Therefore, due to the lack of sequence members, no asymptotic period spacings could be calculated for the $l = 2$ sequence.

Mode Identification. In summary, I used rotationally induced frequency splittings and asymptotic period spacings to identify 100% of B4's pulsations. Corroboration from both methods of mode identification is observed in 75% of the pulsations; these results are presented in Table 4.

B5: KIC 2437937

For B5, I was able to extract 13 frequencies in addition to the recovery of 100% of the pulsations detected by Reed et al. (2012).

Rotationally Induced Frequency Multiplets. Similar to B3, Reed et al. (2012) found no frequency splittings were found. Even using the entire *Kepler* data set of B5, the FT of B5 was particularly sparse of frequency splittings in comparison to our other two targets. I detected only three splittings (0.098, 0.096, and 0.077 μHz), one of which is presented in Figure 30 with the average normalized amplitudes of all three plotted in Figure 31. These frequency splittings all have components whose amplitudes are in the lowest 63% of pulsations. Mode identifications based on these frequency splittings would be tentative, and, as such, primary evidence through asymptotic period spacings is needed in order to properly identify pulsation modes.

Table 4: Pulsation frequencies of B4. Italicized frequencies were prewhitened. The first three columns give the pulsation ID's, frequency, and period with the errors given in parentheses. Columns 4 and 5 are the pulsation amplitude in ppt and in relation to detection thresholds (S/N). Columns 6 and 7 give the ratio (in percent) of the change in period to the period spacing for a given degree-*l* to denote the deviations from asymptotic model sequences. Columns 8-10 give the mode identifications from our results. Column 11 gives the frequency splittings.

ID	Frequency μHz	Period Seconds	S/N	Amplitude ppt	$\Delta P/\Delta\Pi_{l=1}$ %	$\Delta P/\Delta\Pi_{l=2}$ %	*l*	*m*	*n*	Δν μHz
f1	*29.0441 (0.0002)*	*34430.401 (0.193)*	222.57	13.763						
f2	*58.0894 (0.0013)*	*17214.845 (0.393)*	26.68	1.650						
f3	130.8240 (0.0003)	7643.86 (0.02)	4.74	0.293	-7.8		1	-	28	
f4	130.864 (0.001)	7641.52 (0.08)	6.35	0.393	-8.7		1	-	28	
f5	*216.2819 (0.0016)*	*4623.596 (0.033)*	22.66	1.401	11.9		1	-1	15	0.611
f6	216.893 (0.002)	4610.57 (0.04)	9.70	0.600	6.7		1	0	15	0.596
f7	217.489 (0.002)	4597.93 (0.03)	11.42	0.706	1.7		1	1	15	
f8	229.606 (0.001)	4355.2 (0.02)	10.44	0.646	-0.9		1		14	
f9	241.517 (0.002)	4140.50 (0.04)	13.03	0.806	7.6		1		13	
f10	273.484 (0.003)	3656.52 (0.03)	4.63	0.286	2.9		1		11	
f11	290.444 (0.002)	3443.00 (0.02)	7.54	0.466	11.9		1	-1	10	1.268
f12	291.712 (0.004)	3428.04 (0.04)	15.19	0.940	5.9		1	1	10	
f13	316.835 (0.003)	3156.22 (0.03)	12.45	0.770	-8.3		1	-1	9	1.278
f14	318.113 (0.001)	3143.54 (0.01)	7.28	0.450	-13.4		1	1	9	
f15	342.432 (0.004)	2920.29 (0.03)	6.79	0.420	-8.3		1	-1	8	1.261
f16	343.693 (0.003)	2909.57 (0.03)	3.52	0.218	-12.5		1	1	8	
f17	372.629 (0.003)	2683.63 (0.02)	6.79	0.420	-8.5	1.3	1, 2	-1	7, 12	1.265
f18	373.894 (0.004)	2674.55 (0.03)	10.85	0.671	-12.1	-5.4	1, 2	1	7, 12	
f19	404.775 (0.002)	2470.51 (0.01)	4.36	0.270	0.7		1	-1	6	1.264
f20	406.039 (0.003)	2462.82 (0.02)	2.59	0.160	-2.4		1	1	6	

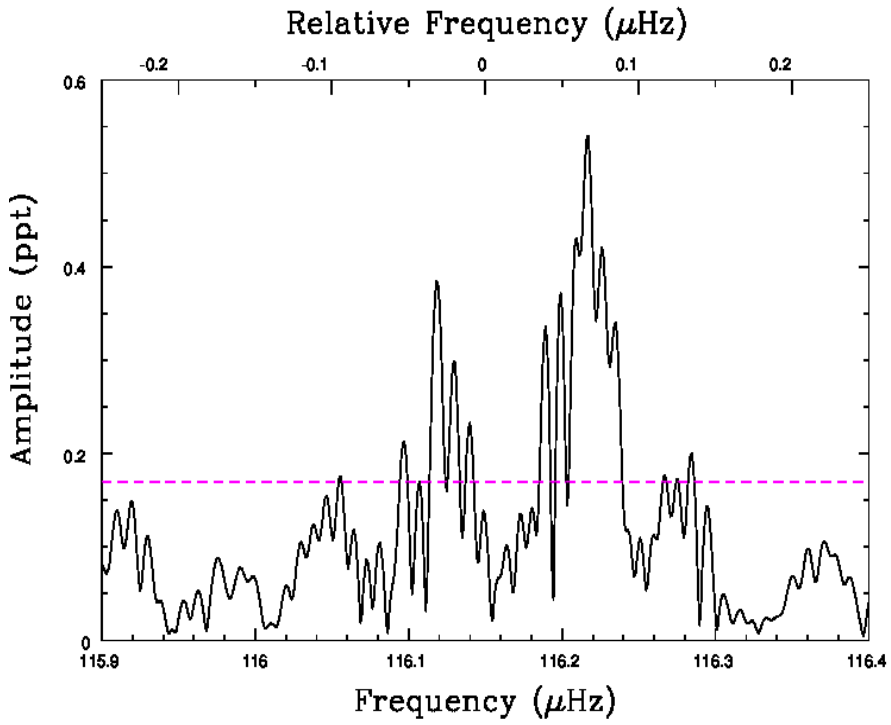

Figure 30: The plot of a frequency multiplet of B5 at 116.217 μHz with a splitting of 0.098 μHz. The dashed magenta line is the detection threshold.

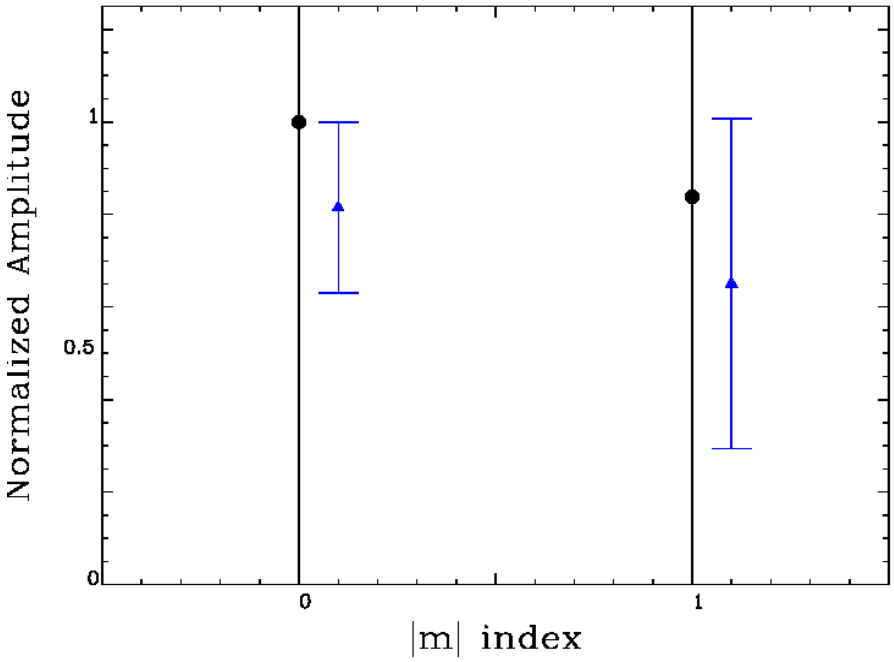

Figure 31: The average, normalized amplitudes for the azimuthal components of the $l = 1$ (black circles) and $l = 2$ (blue triangles) frequency splittings of B5 and their associated error bars.

Asymptotic Period Spacings. Due to the lack of multiplets, identifying pulsation modes in B5 is greatly dependent upon the asymptotic period spacing results. The KS test of B5's pulsations is shown in Figure 32, and the first thing that is noticed is that none of the troughs reach below the 99.9% confidence interval. The deepest trough in the KS test is at ~250 seconds just eclipsing the 99% threshold. For B5, I was able to identify a total of 10 pulsations that lie on the $l = 1$ sequence which has an average period spacing of 248.9 ± 1.3 seconds. This sequence encompasses B5's highest amplitude pulsations which have nearly consecutive radial overtones (n = 6, 8, 9, 10, 11, and 12). Similar to B3 and B4, I used the $l = 1$ sequence to calculate the $l = 2$ sequence and found five pulsations that lie on it; the échelle diagrams of both sequences are presented in Figure 33. The average spacing for the $l = 2$ sequence is 142.66 ± 0.53 seconds. In total, 13 of 17 pulsations were given mode identifications of $l = 1$ and/or 2 using asymptotic period spacings. Similar to B3, there are no remarkable deviations from the asymptotic sequence.

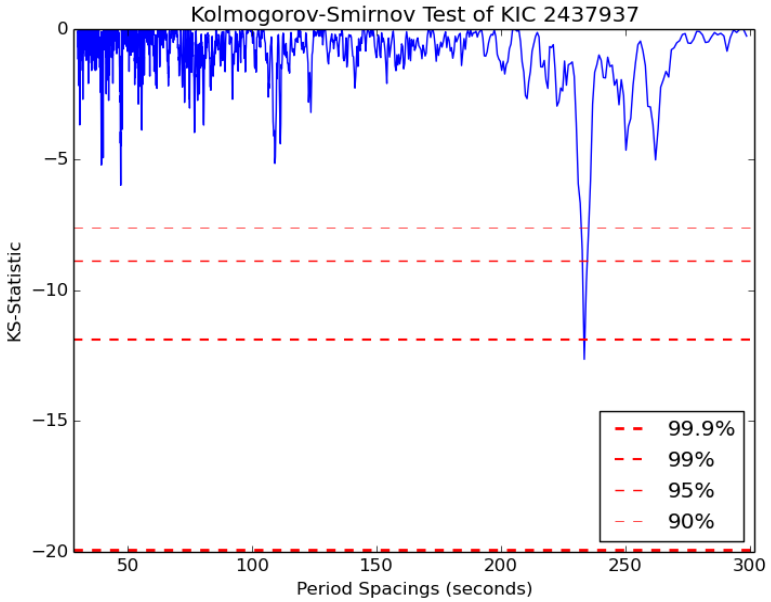

Figure 32: The KS test for B5 plotted with confidence intervals as given in the legend. Note the KS statistic for the $l = 1$ period spacings at just below 250 seconds.

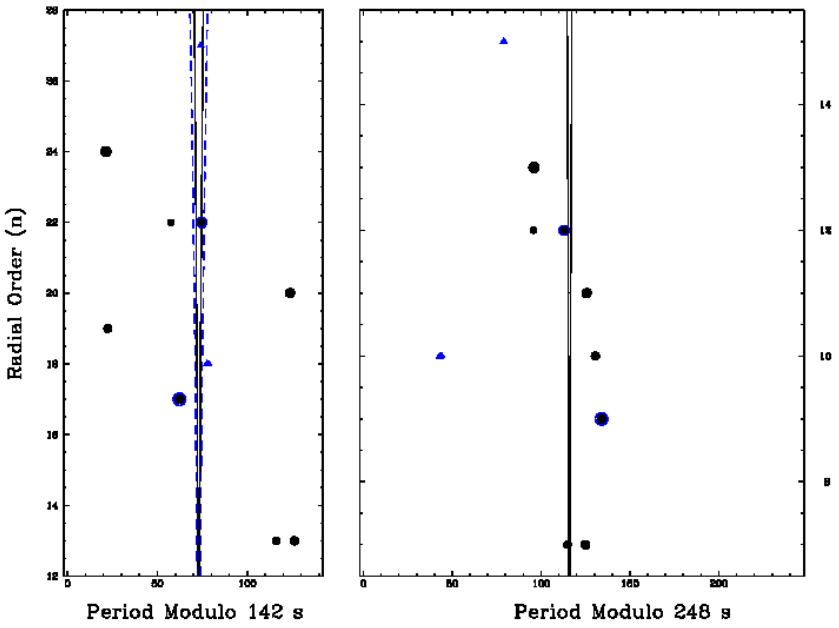

Figure 33: The echelle diagrams of B5 for the l = 1 g-mode pulsation sequence in the right panel, and the l = 2 sequence in the left panel. The black dots identified as l = 1, blue triangles are l = 2, black dots with blue circles are l = 1 and 2, and red asterisks are unknown. The solid lines indicate the calculated position of the m = ±1 components based on the frequency splitting of B5. The dashed lines correspond to the m = ±2 components.

Mode Identification. In summary, I used rotationally induced frequency splittings and asymptotic period spacings to identify 15 pulsation modes of B5; the full list of which is given in Table 5. For B5, the mode identifications are reliant primarily on asymptotic period spacings with only three frequency splittings observed in the entire data set. Two of the multiplets found are on the asymptotic sequence appropriate for their splittings. The third multiplet does not lie on an asymptotic sequence, but has splittings appropriate for l = 2. Three periods are within 10% of the l,n = 1,6 node. There is no way to distinguish between them, so I associate all three frequencies (f15, f16, and f17) with that pulsation mode. In total, I was able to identify a total of 88% of B5's pulsations as l = 1 and/or 2.

Table 5: Pulsation frequencies of B5. Italicized frequencies were prewhitened. The first three columns give the pulsation ID's, frequency, and period with the errors given in parentheses. Columns 4 and 5 are the pulsation amplitude in ppt and in relation to detection thresholds (S/N). Columns 6 and 7 give the ratio (in percent) of the change in period to the period spacing for a given degree-*l* to denote the deviations from asymptotic model sequences. Columns 8-10 give the mode identifications from our results. Column 11 gives the frequency splittings.

ID	Frequency μHz	Period Seconds	S/N	Amplitude ppt	$\Delta P/\Delta\Pi_{l=1}$ %	$\Delta P/\Delta\Pi_{l=2}$ %	*l*	*m*	*n*	Δν μHz
f1	91.405 (0.001)	10940.28 (0.11)	5.85	0.226						
f2	116.119 (0.003)	8611.86 (0.25)	9.90	0.383			2	-1		0.098
f3	116.217 (0.013)	8604.59 (0.98)	10.29	0.398			2	0		
f4	122.395 (0.024)	8170.27 (1.61)	10.56	0.409	-3.9		1		28	
f5	147.953 (0.030)	6758.90 (1.38)	16.85	0.652						
f6	215.557 (0.005)	4639.14 (0.11)	7.49	0.290		-5.7	2		24	
f7	*240.4736 (0.0003)*	*4158.461 (0.004)*	26.72	1.0336	-8.0		1		12	
f8	254.683 (0.006)	3926.45 (0.10)	6.50	0.251	-0.8	0.7	1, 2		11, 19	
f9	255.806 (0.002)	3909.21 (0.03)	4.48	0.173	-7.7		1		11	
f10	*270.9839 (0.0004)*	*3690.256 (0.006)*	15.95	0.6171	4.8		1		10	
f11	*290.1727 (0.0007)*	*3446.223 (0.008)*	10.08	0.3901	7.2		1		9	
f12	297.633 (0.007)	3359.84 (0.08)	5.31	0.205		8.2	2	-1	15	0.096
f13	297.729 (0.006)	3358.76 (0.07)	7.90	0.306		7.5	2	0	15	
f14	312.421 (0.009)	3200.81 (0.09)	14.36	0.556	9.1	-1.9	1, 2		8, 14	
f15	371.200 (0.003)	2693.97 (0.02)	11.78	0.456	6.4		1		6	
f16	372.552 (0.004)	2684.19 (0.03)	5.12	0.198	2.5		1	-1	6	0.077
f17	372.629 (0.002)	2683.63 (0.01)	6.10	0.236	2.3		1	0	6	

RESULTS AND COMPARISONS

From the full *Kepler* data sets, I more than doubled the total known pulsations of B3, B4, and B5. From this expanded list of pulsations I discovered rotationally induced frequency splittings in B3 and B5, mode trapping in B3, and other features which will be discussed in this and the following chapter.

B3: KIC 2569576

From the entire *Kepler* data set of B3 (78% LC data), I detected 30 pulsations in total. I was able to identify 24 out of 27 g-mode pulsations using asymptotic period spacings or frequency splittings. There were ten frequency splittings with an average splitting of 0.090 ± 0.013 μHz. Using the average splitting and equation four on page 17, I calculate the rotation period of B3 to be 64.5 ± 8.2 days, which is normal for a single g-mode sdB star. There are no frequency splittings in the three *p* modes to determine if solid-body or radial differential rotation exists, however, they do fit predicted overtone spacings.

The ratio of observed amplitudes in the azimuthal components of a given multiplet are affected by the inclination of the pulsation axis of a star (Pesnell 1985). I normalized the azimuthal components of the multiplets to the $m = 0$ component, and under the assumption of intrinsically similar amplitudes, I calculated constraints on the inclination axis. Our results indicate an inclination axis of $i < 62°$ from the $m = 0$ component with no constraint from the $m = \pm 1$ component (shown in Figure 34).

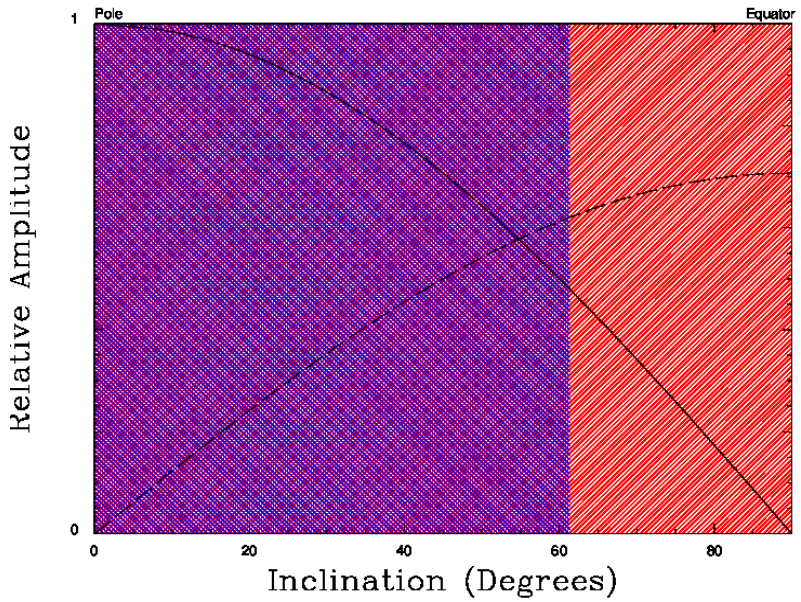

Figure 34: Inclination constraints for B3 are plotted on the Legendre polynomials of degree $l = 1$. The $m = 0$ component is given by the solid line with its constraint shaded in blue. The $m = \pm 1$ component is given by the dashed line and the red shaded constraints. Note the overlap in constraints excludes nearly equator on inclinations.

The asymptotic period spacings of the $l = 1$ sequence in B3 has more members than the $l = 2$, encompassing 65% of the total pulsations. The average spacings of the $l = 1$ sequence is 252.27 seconds and is nearly continuous from $n = 8$ to 17. Above $n = 17$, the sequence is greatly disrupted and only includes two overtones at $n = 22$ and 27. However, evidence of mode trapping is observed at 138.862 μHz. From Table 3, the pulsations f5 and f6 are of relatively high amplitude (S/N ~9 and ~28, respectively), and exhibit a frequency splitting of 0.108 μHz. From the splitting I can identify it as an $l = 1$ mode, however, it is trapped completely off of the $l = 1$ period sequence (shown in the right panel of Figure 25 close to $n = 25$). The sequence is discontinuous in this region though (as shown in the reduced period plot in Figure 35), and there is no pulsation detected where the corresponding trapped l, $n = 2, 25$ would be.

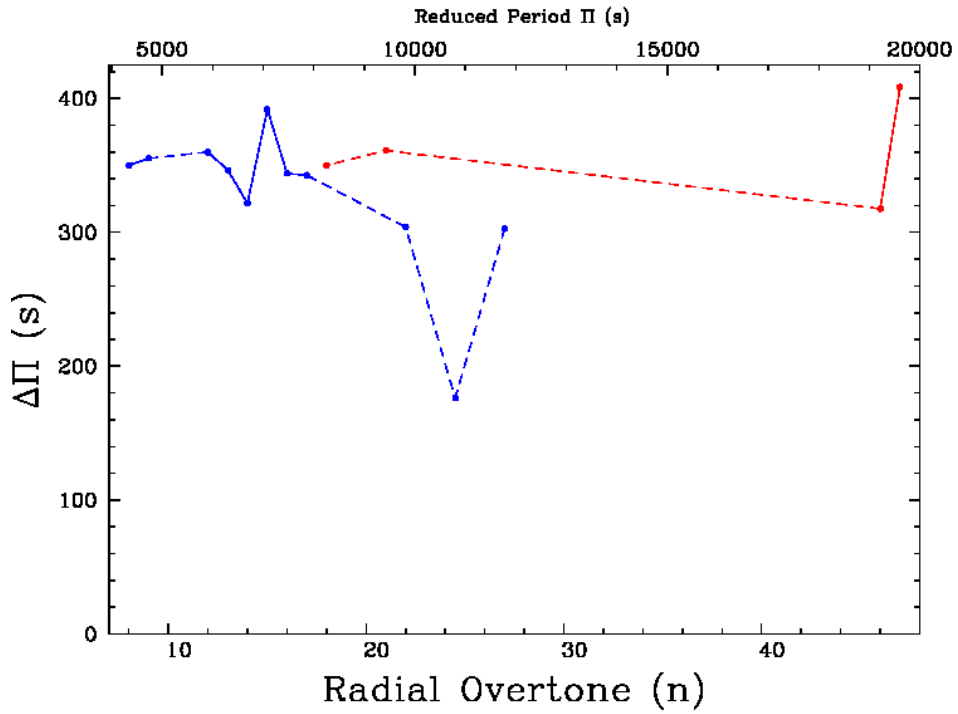

Figure 35: Reduce period plot of B3. Blue points and lines represent the l = 1 sequence while the red points and lines represent the l = 2 sequence. Solid lines indicate continuous radial overtones while dashed lines indicate missing sequence members.

B4: KIC 2438324

From B4's entire *Kepler* data set (73% SC data), I detected 20 pulsations in total including the orbital alias and its overtone (f1 and f2 from Table 4). Of the pulsations, 100% were identified with low-degrees ($l \leq 2$) using asymptotic period spacings and frequency splittings. There were seven frequency splittings with an average splitting of 0.629 ± 0.012 μHz from which I calculate the rotation period to be 9.21 ± 0.18 days. This is slightly short, but not unusual for an sdB + M-dwarf system. Like B3, I can determine the inclination constraints from the l = 1 Legendre polynomials and the relative amplitudes of the components of B4's multiplets shown in Figure 27. The constraints of each azimuthal component overlap at high inclination angles (shown in Figure 36) which

provide a lower bound ($i > 76°$) for the inclination axis. An upper bound can be determined from the geometric arrangement of potential binary companions, which exclude eclipses. Using Kepler's 3rd law and the known sdB radius of 0.2 $R_\odot$, I determine that the upper bound is 83.5° for the edge of the companion's stellar surface to eclipse the sdB. The true inclination will depend upon the radius of the companion.

Every one of the frequency splittings used to constrain the pulsation axis occur on the $l = 1$ period sequence. There is a nearly continuous portion of the sequence which is only missing one member ($n = 12$) from $n = 6$ to 15, and it also has the characteristic hook feature seen in many other sdB period sequences (shown in Figure 29). However, B4's hook feature meanders left at low radial orders, which is opposite what is normally observed (Baran & Winans, 2012). In congruence with the continuity in overtones on the sequence, no trapped modes are found.

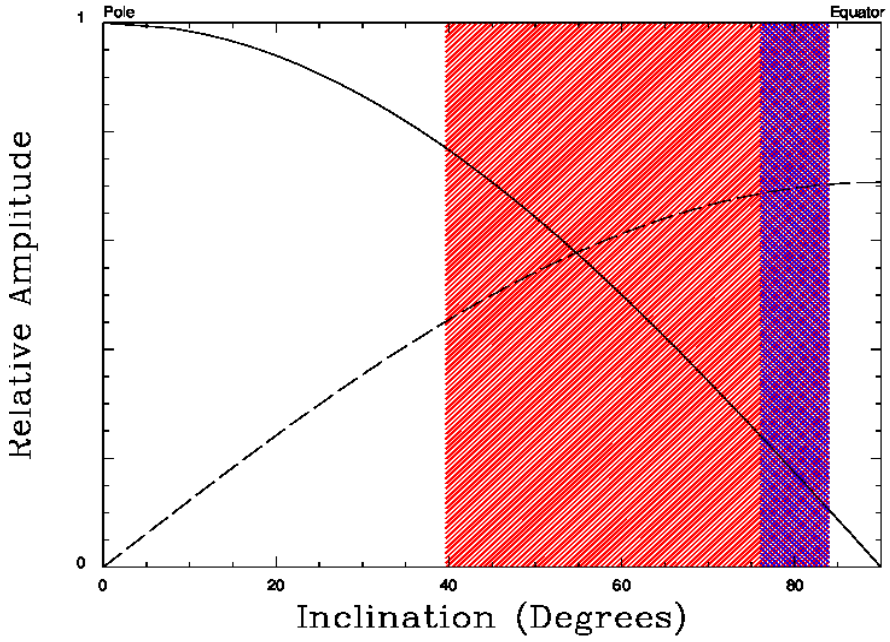

Figure 36: Inclination constraints for B4 are plotted on the Legendre polynomials of degree-$l = 1$. The $m = 0$ component is given by the solid line with its constraint shaded in blue. The $m = \pm 1$ component is given by the dashed line and the red shaded constraints. Note the overlapping region constrains the inclination to be nearly equator on.

B5: KIC 2437937

From the entire *Kepler* data set of B5 (78% LC data), I detected 17 pulsations in total. I used asymptotic period spacings and frequency splittings to identify 88% of these with low-degree ($l \leq 2$) modes. The only $l = 1$ splitting of 0.077 ± 0.004 μHz gives a rotation period of 75.2 ± 3.7 days. The $l = 2$ multiplets have an average splitting of 0.097 ± 0.016 μHz from which I derive a rotation period of 99.4 ± 14.0 days. While these are not the same, at the 1σ level, they both indicate a long rotation, which is normal for a single g-mode pulsator. I simply average them together for a rotation period of 91.3 ± 14.1 days.

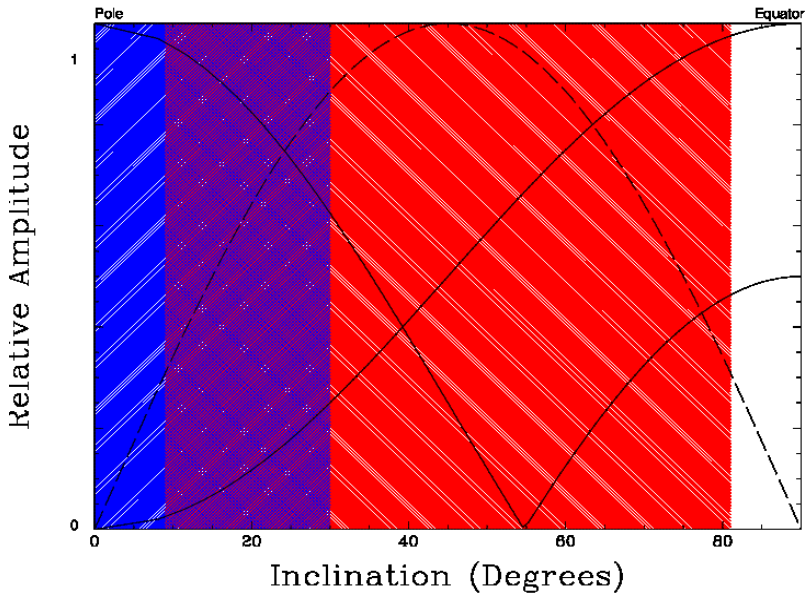

Figure 37: Inclination constraints for B5 are plotted on the Legendre polynomials of degree $l = 2$. The $m = 0$ and ±2 components are given by the solid line with the $m = 0$ constraint shaded in blue. The $m = \pm 1$ component is given by the dashed line and the red shaded constraints.

I determined inclination constraints using the $l = 2$ multiplets. The result is an inclination between 8° and 30° (Figure 37). The $l = 1$ multiplet did not constrain the inclination as it had excessive amplitude variations. With such few splittings, asymptotic

period spacings were necessary for mode identifications. From our linear regression fits I determined period spacings of 248.9 and 142.66 seconds for the l = 1 and 2 sequences, respectively. The single l = 1 frequency splitting fell on the l = 1 sequence at n = 6. Coincidentally this doublet is the start of a nearly continuous sequence from n = 6 to 12 which is missing only n = 7. The sequence is primarily concentrated at low radial orders and shows no significant deviations from the asymptote.

Comparisons

To determine any similarities or differences between B3, B4, and B5, I analyze the atmospheric and asteroseismic properties determined for each. Comparing the total number of pulsations with the atmospheric parameters, I see that there are no clear trends in either effective temperature or surface gravity (shown in Figures 38 and 39, respectively). Low and high temperature stars can have single digit quantities to multiple hundreds of pulsations. Perhaps I see an effect with the higher surface gravity sdBs having fewer pulsations, however, this trend should be compared with model instability predictions.

The faintness of the objects lowers the amplitude of the pulsations in the FT, and could affect the quantity of pulsations I detect; a plot of total pulsations with *Kepler* magnitudes is shown in Figure 40. Most of the pulsators have quantities from single digits to 70 pulsations with magnitudes from K_p =18 to 13.5. If the magnitude affected the quantities of detected pulsations, then I would expect there to be some decrease in the total number of pulsations as the stars become fainter. I do not see this trend, however, there are no pulsators over 17th magnitude with hundreds of pulsations. Some *Kepler*

targets from the main mission have not had analyses of their entire data sets, after which more appropriate comparisons can be made.

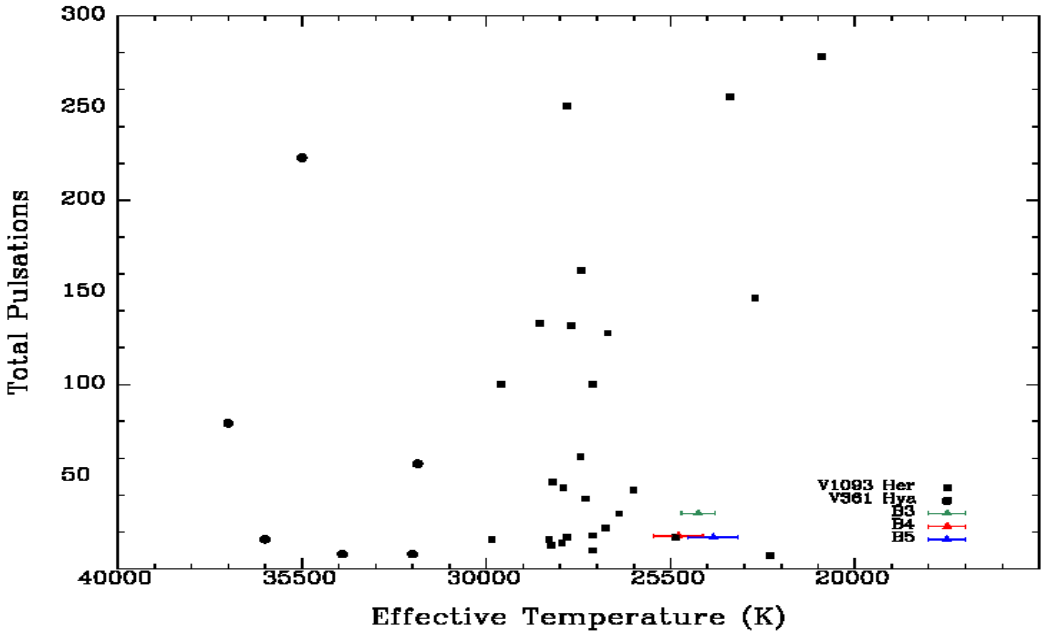

Figure 38: The total pulsations plotted against the effective temperature of known *Kepler* sdB pulsators including B3 (green), B4 (red), and B5 (blue) with their associated error bars.

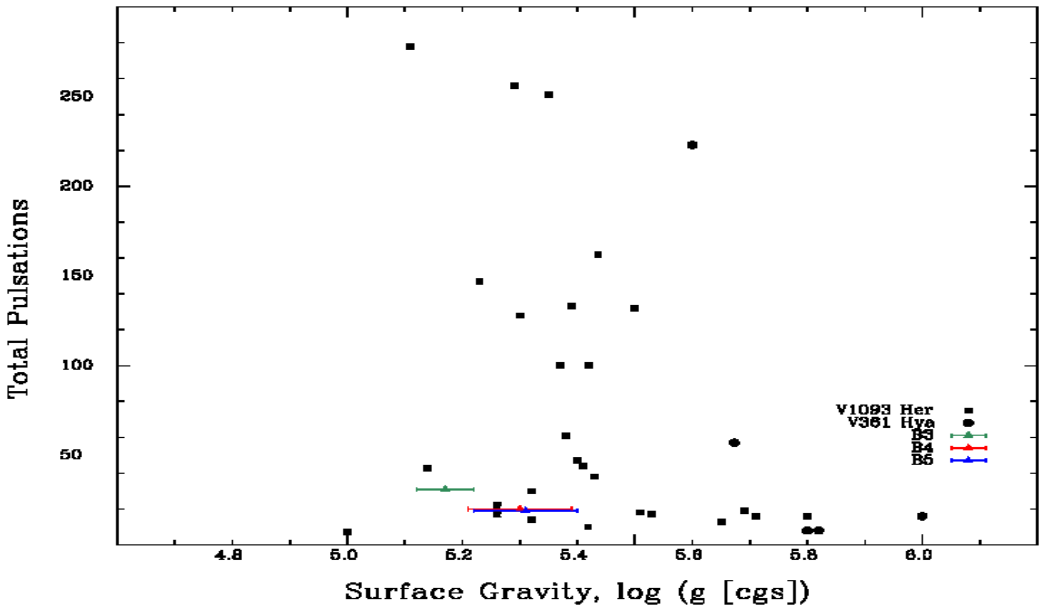

Figure 39: The total pulsations plotted against the surface gravity of known *Kepler* sdB pulsators including B3 (green), B4 (red), and B5 (blue) with their associated error bars.

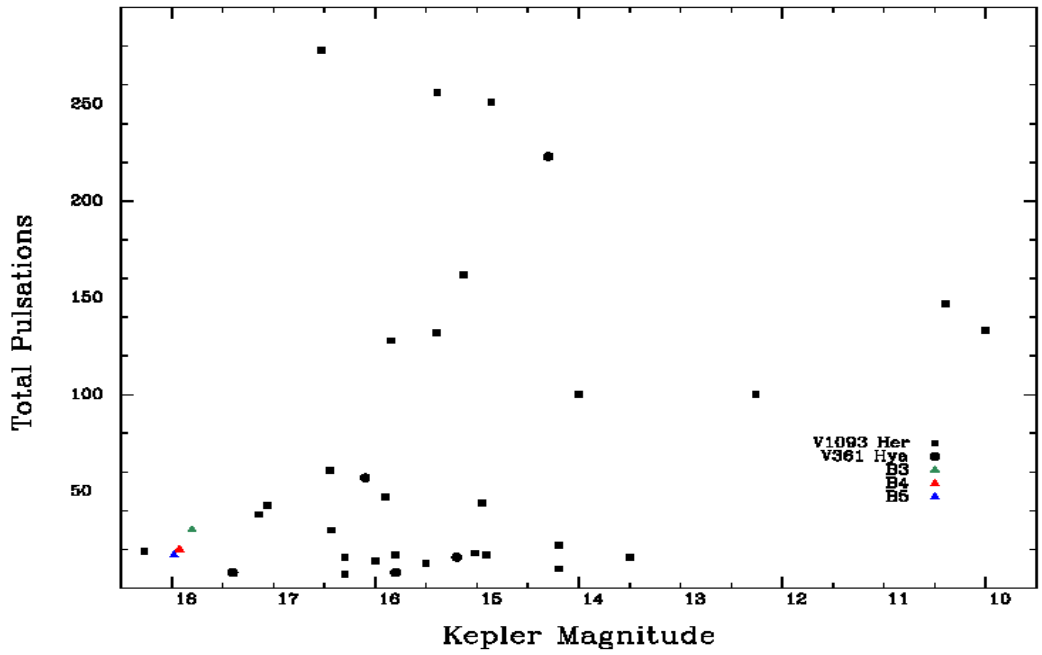

Figure 40: The total pulsations plotted against the *Kepler* magnitude of known *Kepler* sdB pulsators including B3 (green), B4 (red), and B5 (blue).

In sdB evolution, their rotation periods can be perturbed by interactions with binary companions. There seems to be a trend in B3, B4, and B5 such that as the effective temperature increases, the rotation period decreases (shown in Figure 41) even though the rotation period of B4 is likely affected by its M-dwarf counterpart. Perhaps the common envelope phase of B4 and its companion allowed for more of B4's hydrogen envelope to be stripped, creating a slightly hotter sdB with a faster rotation period. In general, the trend is also seen with all of the *Kepler* sdBs (Reed et al., 2014). The hotter, p-mode pulsators all have faster rotation periods of less than 30 days, while the cooler, g-mode pulsators can have rotation periods upwards of 100 days. The trend is seen slightly with rotation period compared to the surface gravity of known *Kepler* sdBs which is shown in

Figure 42. As the surface gravity increases, the rotation period decreases, however, at low surface gravities there are sdBs with rotation periods less than 10 days and close to 100 days.

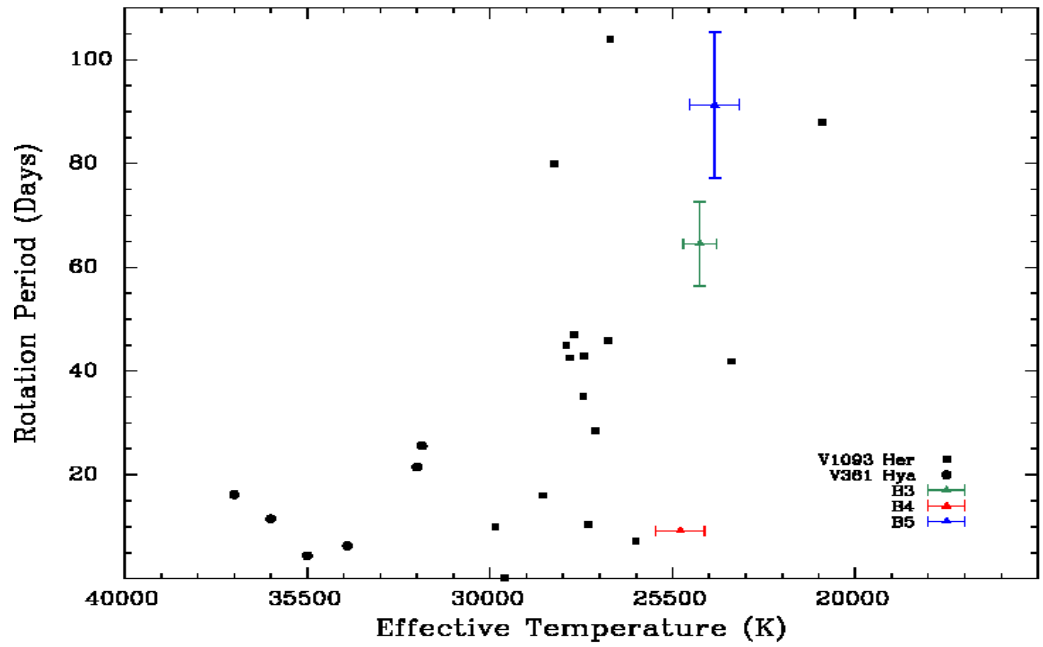

Figure 41: Rotation period plotted against the effective temperature of known *Kepler* sdB pulsators including B3 (green), B4 (red), and B5 (blue) with their associated error bars.

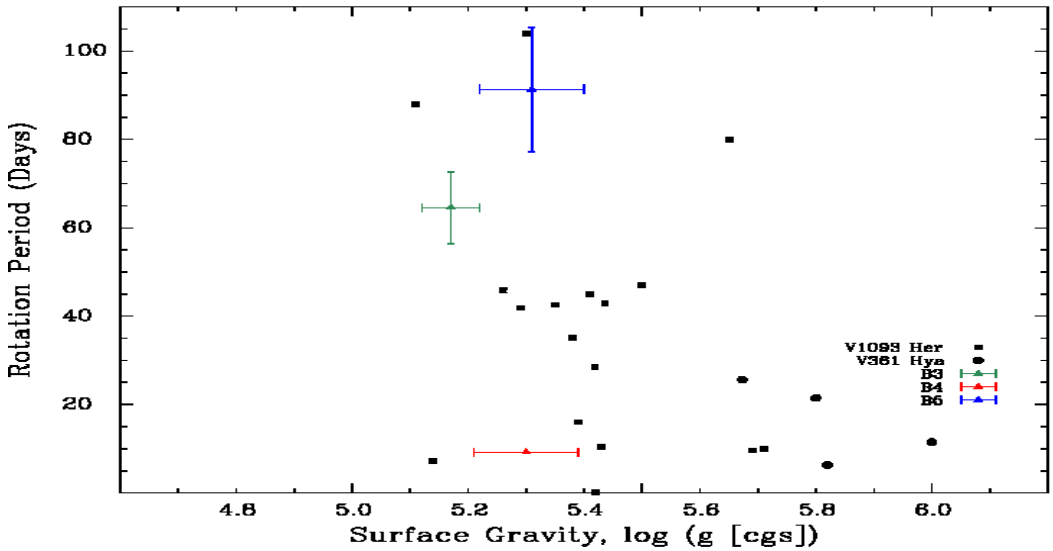

Figure 42: Rotation period plotted against the surface gravity of known *Kepler* sdB pulsators including B3 (green), B4 (red), and B5 (blue) with their associated error bars.

Period spacings were compared with effective temperature and surface gravity (shown in Figure 43 and 44). There are no trends with surface gravity, however, they seem to be two diagonal groupings with effective temperature. These groupings should be explored when analysis of all Kepler sdBV stars is complete. In general, the period spacings group together around a weighted average value of 251.22 ± 0.08 seconds.

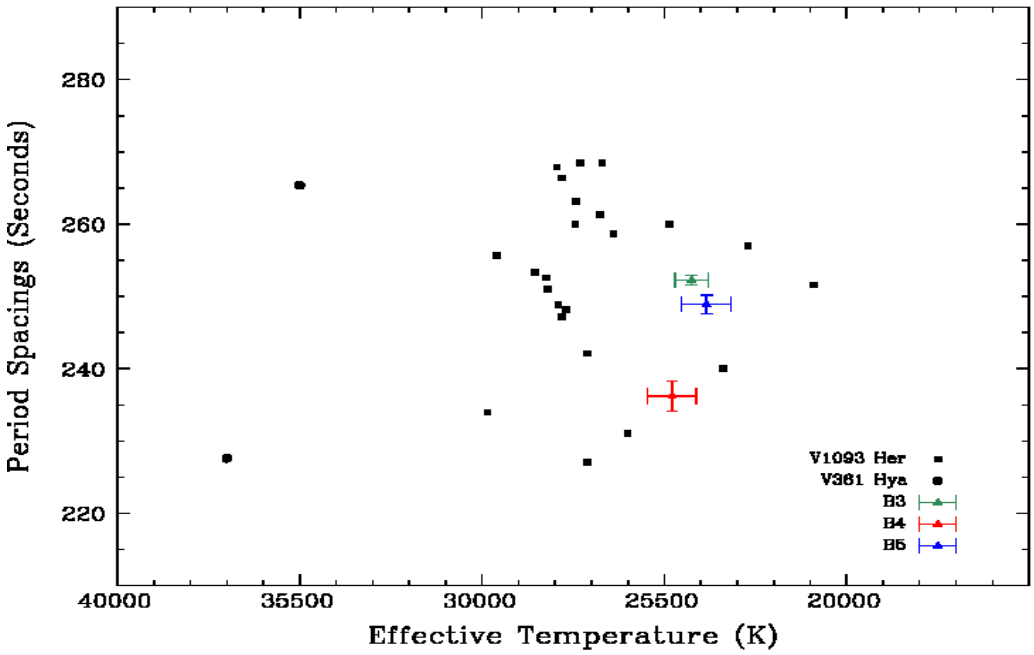

Figure 43: Period spacings plotted against the effective temperature of known *Kepler* sdB pulsators including B3 (green), B4 (red), and B5 (blue) with their associated error bars.

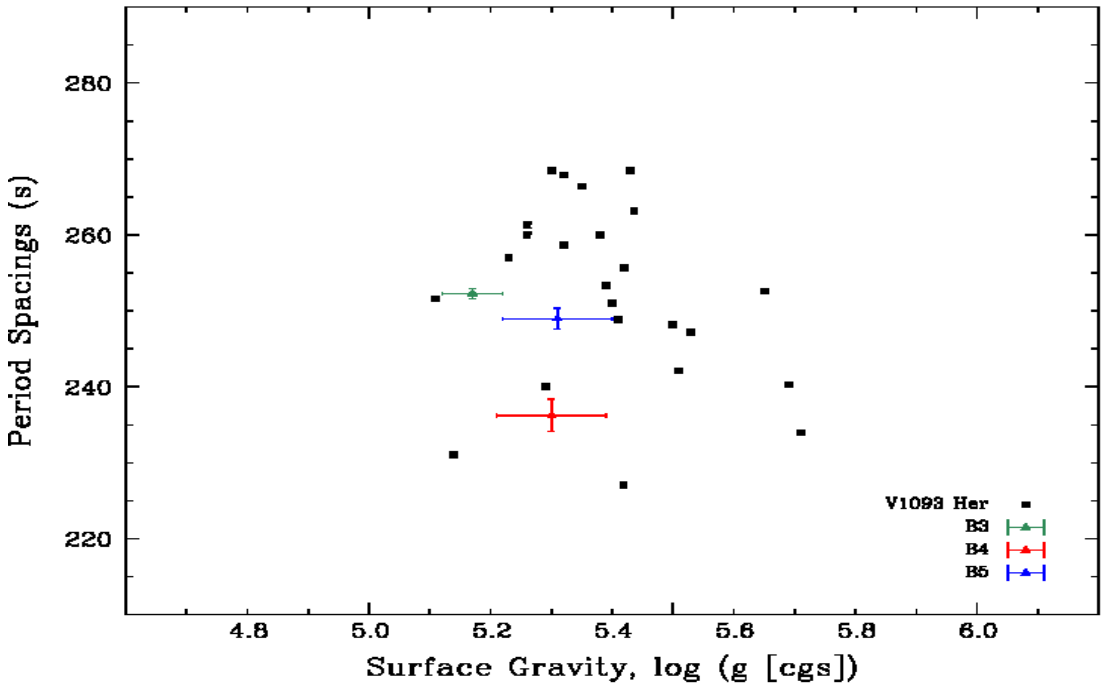

Figure 44: Period spacings plotted against the surface gravity of known *Kepler* sdB pulsators including B3 (green), B4 (red), and B5 (blue) with their associated error bars.

DISCUSSION

NGC 6791 is a unique open cluster. Its high metallicity ([Fe/H] ≈ +0.40; Carraro et al., 2006) and old age (7 Gyr; Anthony-Twarog et al., 2007) put the cluster on the upper limits of age and metallicity for open clusters. The most recent photometric study performed by Anthony-Twarog, Twarog and Mayer in 2007 resulted in an updated detailed analysis of the color-magnitude diagram (CMD) of NGC 6791. From the CMD, all of the stars fall on a smooth evolutionary track with a turnoff at roughly B-V ≈ 0.68 as shown in Figure 45.

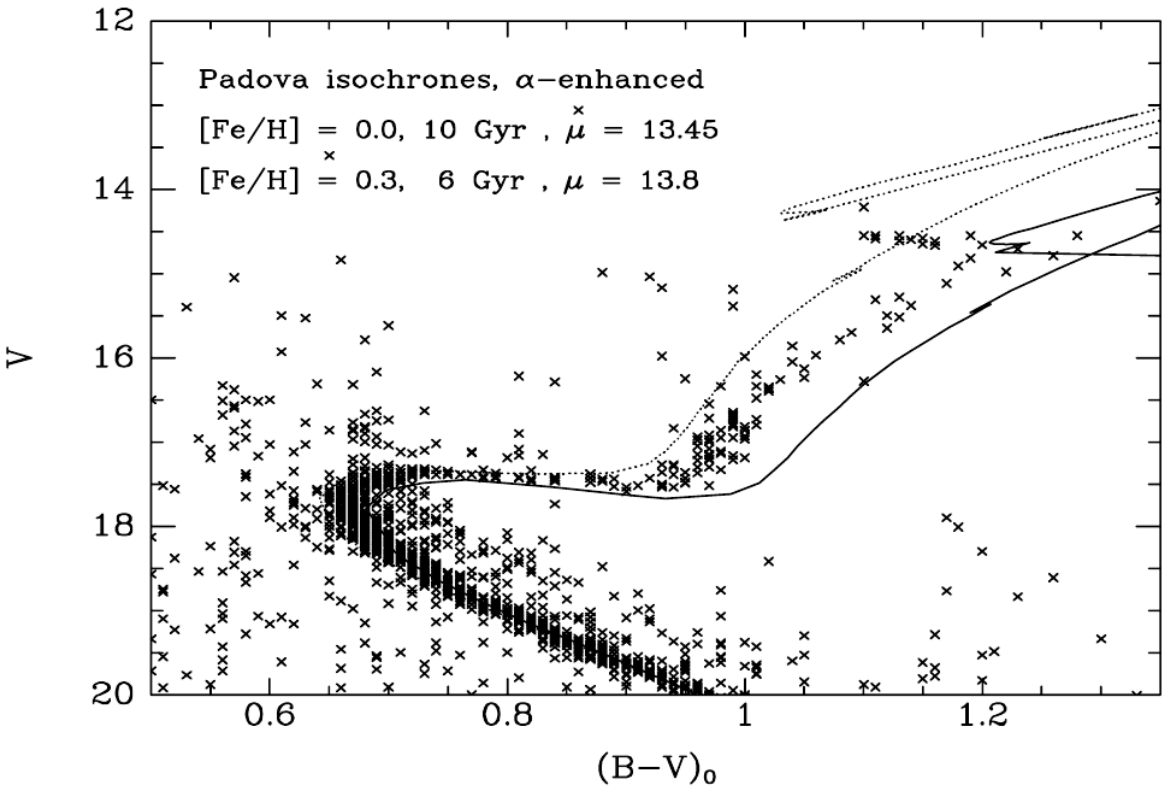

Figure 45: CMD for NGC 6791 with isochrones for Fe/H = 0.0 (dotted line) and 0.3 (solid line) of Girardi et al. (2002). *Credit: Stetson et al., 2003; Anthony-Twarog et al., 2007.*

If multiple star formation epochs occur within the same cluster, then stars formed in separate epochs would form independent sequences on the CMD. This is not seen in the CMD of NGC 6791. The smooth distribution of stars on the CMD implies that all of the stars were born in a single formation epoch, which is important in the determination of turn-off masses and can affect the interpretation of the asteroseismic and atmospheric properties of B3, B4, and B5. Stars that are in the same stage of evolution and are part of the same cluster (like B3, B4, and B5) have the same age, progenitor mass, initial metallicity, and preferred inclination within the cluster. Since they have such similar beginnings, any differences in their current states are due to their unique formation scenarios.

The T_{eff}-log *g* plot in Figure 14 shows that B3, B4, and B5 all fall within the range of g-mode pulsators, and all of the pulsations in all three stars *are* g-mode pulsations except for three *p* modes in B3. The total number of pulsations for each star were low compared to other *Kepler* sdBs. In particular, B4 had the most SC data (Q06 through Q17), which I expected to have the most pulsations but ended up not being the case. The amount of SC data I obtained for B4 was roughly equal to that of KIC 2697388 and KIC 11558725, which both had roughly 250 pulsations each; ten times the amount I detected in B4. However, both KIC 2697388 and KIC 11558725 are nearly three magnitudes brighter (15.39 and 14.95, respectively) than B4, so, the small amount of pulsations from the full *Kepler* data sets of all three stars could be an effect of their faint magnitudes (see Figure 40).

I was able to discover rotation periods for B3 (64.5 ± 8.2 days) and B5 (91.3 ± 14.1 days), as well as confirm the rotation period of B4 (9.21 ± 0.18 days). B4 is in a

short-period reflection-effect binary ($P_{orb} \approx 0.398$ days; Pablo et al., 2011), and is rotating slower than its companion orbits. Short-period binaries go through a common envelope phase where angular momentum in the system is transferred to the common, filled Roche lobe in order to heat and eject it. For B4, this resulted in a slightly hotter sdB than B3 and B5, and a much faster rotator. So, B3 and B5's long rotation periods suggests that they can be excluded from being in a short-period binary.

The rotation period of B4 is likely spun-up by its binary companion, and it is no considerable surprise that B3 and B5's rotation periods are much longer due to their lack of apparent binarity. This could be a product of their closer proximity to the cluster's center (B3, 199" and B5, 123" compared to B4, 236") and the tidal disruptions that are experienced there. The binary companion of B4 has also perturbed the inclination of B4 ($76° < i < 84°$) from the preferred inclination ($20° < i < 30°$) of the other cluster members who have had their angular momentum exchanged with only the progenitor molecular cloud (Corsaro et al., 2017). This is not the case for B3 and B5. The inclination of B3 is constrained to less than 62° and B5's is constrained from 8° to 30°, both overlapping the preferred inclination of solar-like oscillators which is 20° to 30° (Corsaro et al., 2017). This is more evidence that these stars truly do not have binary partners, because they are not perturbed from their original inclinations as RG stars. Their long rotation periods also suggest that they can be excluded from being in a short-period binary.

One unique feature of B3 is that it shows signs of mode trapping. These trapped modes are thought to be caused by pulsations which pass over the sharp C-O/He boundary in the core. More specifically, convective overshoot at this transition layer has

been shown to result in trapped modes (Constantino et al., 2015; Ghasemi et al., 2017). The fact that B3 exhibits mode trapping where B4 and B5 do not may indicate that there is increased diffusion which smoothed this boundary in B4 and B5 (Constantino et al., 2015; Ghasemi et al., 2017).

There are other similarities between B3 and B5, though. They are both long-period rotators and have $l = 1$ period spacings close to 250 seconds. Comparing the period spacings of B3, B4, B5 and the other *Kepler* sdBs (251.22 seconds) to that of the RC stars (268.5 seconds) in NGC 6791, I see that as surface gravity decreases the period spacing values increase, but only by 6.8%. Since RC stars are HB stars, they have begun fusing helium, so their core masses must have been similar to that of the sdB progenitor's near the tip of the RGB considering the helium flash occurs at the same core mass (0.47 $M_{\odot}$). Although RC stars and sdB stars have the same progenitor mass, one major difference between RC stars and sdB stars is the thickness of the hydrogen envelope, and is a consequence of the overall mass loss in the system. This can affect the resultant star's rotation period and inclination, but apparently does little to affect period spacing values. This implies that period spacings are more strongly dictated by core mass than overall mass.

Future work could be done to confirm the inclination of the B4 binary system which will give insight into how the angular momentum from the cluster preferred inclinations was transferred throughout its mass loss on the RGB. A high resolution spectroscopic analysis of B4 could be performed in order to produce radial velocity curves from which the inclination of the binary partner can be calculated, although this is difficult due to how faint the star is. For B3 and B5, detailed asteroseismic models could

be developed to replicate their sequences, especially the mode trapping in B3.

Also, because the distance to the clusters is known through various methods, the radii and masses of B3, B4, and B5 can be calculated if a precise absolute luminosity could be determined using surveys with small flat-field uncertainties and accurate color-based flux calibrations like SDSS. The lifetimes of solar-mass stars in general are on the order of $\sim 10^{10}$ years, and their lives on the HB are $\sim 10^{8}$ years. Since there was only one star formation epoch in NGC 6791 and such a short amount of time is spent on the HB, this implies that the sdB progenitors had to have had identical masses, which can be roughly estimated from the masses of turn-off stars (1.15 $M_{\odot}$; Brogaard et al., 2011). If the mass and radii of B3, B4, and B5 could be calculated, this would give insight into the progenitor's mass loss after the main sequence.

REFERENCES

Aerts, C., Christensen-Dalsgaard, J., & Kurtz, D. W. (2010). *Asteroseismology.* New York, NY: Springer.

An, D., Terndrup, D. M., Pinsonneault, M. H., & Lee, J. W. (2015). The distances to open clusters from main-sequence fitting. V. Extension of color calibration and test using cool and metal-rich stars in NGC 6791. *The Astrophysical Journal, 811(1)*.

Anthony-Twarog, B. J., Twarog, B. A., & Mayer, L. (2007). vbyCaHβ CCD photometry of clusters. VIII. The super-metal-rich, old open cluster NGC 6791. *The Astronomical Journal, 133(4)*, 1585-98.

Baran, A. S., & Winans, A. (2012) Mode Identification of Three Pulsating Subdwarf B Stars via Multiplets and Period Spacing. *Acta Astronomica, 62(4),* 343-55.

Baran, A. S., Reed, M. D., Østensen, R. H., Telting, J. H., & Jeffery, C. S. (2017). EPIC 211779126: a rare hybrid pulsating subdwarf B star richly pulsating in both pressure and gravity modes. *Astronomy and Astrophysics, 597*, A95.

Basu, S., Grundahl, F., Stello, D., Kallinger, T., Hekker, S., Mosser, B., Garcia, R., . . . Smith, J. C. (2011). Sounding open clusters: Asteroseismic constraints from *Kepler* on the properties of NGC 6791 and NGC 6819." *The Astrophysical Journal Letters, 729(1)*, L10.

Bevington P. R., & Robinson, D. K. (2003). *Data reduction and error analysis for the physical sciences.* New York, NY: McGraw-Hill.

Bordé, P., Rouan, D., & Leger, A. (2003). Exoplanet detection capability of the COROT space mission. *Astronomy and Astrophysics, 405*, 1137-44.

Bossini, D., Miglio, A., Salaris, M., Vrard M., Cassisi, S., Mosser, B., Montalban, J., . . . Tayar, J. (2017). *Kepler* red-clump stars in the field and in open clusters: constraints on core mixing. *Monthly Notices of the Royal Astronomical Society, 469,* 4718-25.

Brogaard, K., Bruntt, H., Grundahl, F., Clausen, J. V., Frandsen, S., VandenBerg, D. A., & Bedin, L. R. (2011). Age and helium content of the open cluster NGC 6791 from multiple eclipsing binary members I: Measurements, methods, and first results. *Astronomy and Astrophysics, 525*, A2.

Caloi, V. (1989). Evolution of extreme horizontal branch stars. *Astronomy and Astrophysics, 221*, 27-35.

Carraro, G., Villanova, S., Demarque, P., Virginia McSwain, M., Piotto, G., & Bedin, L. R. (2006). NGC 6791: An exotic open cluster or the nucleus of a tidally disrupted galaxy? *The Astrophysical Journal Letters, 643*, 1151-59.

Charpinet, S., Fontaine, G., Brassard, P., & Dorman, B. (1996). The potential of asteroseismology for hot, subdwarf B stars: A new class of pulsating stars? *The Astrophysical Journal Letters, 471(2)*, L103-06.

Charpinet S., Fontaine, G., Brassard, P., Chayer, P., Rogers, F. J., Iglesias, C. A., & Dorman, B. (1997). A driving mechanism for the newly discovered class of pulsating subdwarf B stars. *The Astrophysical Journal Letters, 483(2)*, L123-26.

Charpinet, S., Fontaine, G., Brassard, P., & Dorman, B. (2002). Adiabatic survey of subdwarf B star oscillations. III. Effects of extreme horizontal branch stellar evolution on pulsation modes. *The Astrophysical Journal Supplement Series, 140*, 469-561.

Charpinet, S., Van Grootel, V., Reese, D., Fontaine, G., Green, E. M., Brassard, P., & Chayer, P. (2008). Testing the forward modeling approach in asteroseismology. II. Structure and internal dynamics of the hot B subdwarf component in the close eclipsing binary system PG 1336-018. *Astronomy and Astrophysics, 489*, 377-94.

Constantino, T., Campbell, S., Christensen-Dalsgaard, J., Lattanzio, J., & Stello, D. (2015). The treatment of mixing in core helium burning models – I. Implications for asteroseismology. *Monthly Notices of the Royal Astronomical Society, 452*, 123-145.

Copperwheat, C. M., Morales-Reda, L., Marsh, T. R., Maxted, P. F. L., & Heber, U. (2011). Radial-velocity measurements of subdwarf B stars.*Monthly Notices of the Royal Astronomical Society, 415*, 1381-95.

Corsaro, E., Lee, Y., Garcia, R. A., Hennebelle, P., Mathur, S., Beck, P., Mathis, S., . . . Bouvier, J. (2017). Spin alignment of stars in old open clusters. *Nature Astronomy*, *1*, 0064.

Cunha, M. S., Aerts, C., Christensen-Dalsgaard, J., Baglin, A., Bigot, L., Brown, T. M., Catala, O. L., . . . Thompson, M. J. (2007). Asteroseismology and interferometry. *The Astronomy and Astrophysics Review*, *14*, 217-360.

D'Cruz, N. L., Dorman, B., Rood, R. T., & O'Connell, R. W. (1996). The origin of extreme horizontal branch stars. *The Astrophysical Journal, 466*, 359.

De Marchi, D., Poretti, E., Montalto, M., Piotto, G., Desidera, S., Bedin, L. R., Claudi, R., . . . Stetson, P. B. (2007). Variable stars in the open cluster NGC 6791 and its surrounding field. *Astronomy and Astrophysics, 471*, 515-26.

Downes, R. A. (1986). The KPD survey for galactic plane ultraviolet-excess objects Space densities of white dwarfs and subdwarfs. *The Astrophysical Journal Supplement Series, 61*, 569-84.

Fontaine, G., Brassard, P., Charpinet, S., Green, E. M., Chayer, P., Billeres, M., & Randall, S. K. (2003). A Driving Mechanism for the Newly Discovered Long-Period Pulsating Subdwarf B Stars. *The Astrophysical Journal, 597*, 518-34.

Fontaine, G., Brassard, P., Charpinet, S., Green, E. M., Randall, S. K., & Van Grootel, V. (2012). A preliminary look at the empirical mass distribution of hot B subdwarf stars. *Astronomy and Astrophysics, 539*, A12.

Foster, H., Reed, M. D., Telting, J. H., Østensen, R. H., & Baran, A. S. (2015). The discovery of differential radial rotation in the pulsating subdwarf B star KIC 3527751. *The Astrophysical Journal, 805*, 94.

Ghasemi, H., Moravveji, E., Aerts, C., Safari, H., & Vuckovic, M. (2017). The effects of near-core convective shells on the gravity modes of the subdwarf B pulsator KIC 10553698A. *Monthly Notices of the Royal Astronomical Society, 465*, 1518-31.

Green, R. F., Schmidt, M., & Liebert, J. (1986). The Palomar-Green catalog of ultraviolet-excess stellar objects. *The Astrophysical Journal Supplement Series, 61*, 305-52.

Green, E. M., Fontaine, G., Reed, M. D., Callerame, K., Seitenzahl, I. R., White, B. A., Hyde, E. A., . . . Bronowska, A. (2003). Discovery of a new class of pulsating stars: Gravity-mode pulsators among subdwarf B stars. *The Astrophysical Journal Letters, 583*, L31-34.

Green, E. M., Guvenen, B., O'Malley, C. J., O'Connell, C. J., Baringer, B. P., Villareal, A. S., Carleton, T. M., . . . Charpinet, S. (2011). The unusual variable hot B subdwarf LS IV–14°116. *The Astrophysical Journal, 734*, 59.

Greenstein, G. S. (1967) Helium Deficiency in Old Halo B Stars. *Nature, 213(5079),* 871-73.

Greenstein, J. L., & Sargent, A. I. (1974). The nature of faint blue stars in the halo. II. *The Astrophysical Journal Supplement Series, 28*, 157.

Heber, U., Hunger, K., Jonas, G., & Kudritzki, R. P. (1984). The atmosphere of subluminous B stars. *Astronomy and Astrophysics, 130*, 119-30.

Heber, U. (1986). The atmosphere of subluminous B stars. II - Analysis of 10 helium poor subdwarfs and the birthrate of sdB stars. *Astronomy and Astrophysics, 155*, 33-45.

Heber, U., Reid, I. N., & Werner, K. (2000). Spectral analysis of multimode pulsating sdB stars. II. Feige 48, KPD 2109+4401 and PG 1219+534. *Astronomy and Astrophysics, 363*, 198-207.

Heber, U. (2009). Hot subdwarf stars. *Annual Review of Astronomy and Astrophysics*, *47*, 211-51.

Heber, U. (2016). Hot subluminous stars. *Publications of the Astronomical Society of the Pacific*, *128(966)*.

Humason, M. L., & Zwicky, F. (1947). A search for faint blue stars. *The Astrophysical Journal, 105*, 85.

Jenkins, J. (2002). The impact of solar-like variability on the detectability of transiting terrestrial planets. *The Astrophysical Journal, 575*, 493-505.

Kałuźny, J., & Udalski, A. (1992). Photometric study of the old open cluster NGC 6791. *Acta Astronomica*, *42*, 29-47.

Kałuźny, J., & Rucinski, S. M. (1995). CCD photometry of distant open clusters. II. NGC 6791. *Astronomy and Astrophysics Supplement, 114*, 1-20.

Kasting, J. F., Whitmire, D. P., & Reynolds, R. T. (1993). Habitable zones around main sequence stars. *Icarus*, *101*, 108-28.

Kawaler, S. D., Reed, M. D., Østensen, R. H., Bloemen, S., Kurtz, D. W., Quint, A. C., Silvotti, R., . . . Koch, D. G. (2010). First *Kepler* results on compact pulsators – V. Slowly pulsating subdwarf B stars in short-period binaries. *Monthly Notices of the Royal Astronomical Society, 409*, 1509-17.

Kern, J. W., Reed, M. D., Baran, A. S., Østensen, R. H., & Telting, J. H. (2017). Kepler observations of the pulsating subdwarf B star KIC 2697388: the detection of converging frequency multiplets in the full data set. *Monthly Notices of the Royal Astronomical Society, 465*, 1057-65.

Kern, J. W., Reed, M. D., Baran, A. S., Telting, J. H., & Østensen, R. H. (2018). Asteroseismic analysis of the pulsating subdwarf B star KIC 11558725: an sdB+WD system with divergent frequency multiplets and mode trapping observed by Kepler. *Monthly Notices of the Royal Astronomical Society, 474*, 4709-16.

Kilkenny, D., Koen, C., O'Donoghue, D., & Stobie, R. S. (1997). A new class of rapidly pulsating star - I. EC 14026-2647, the class prototype. *Monthly Notices of the Royal Astronomical Society, 285*, 640-44.

Koch, D. G., Borucki, W. J., Basri, G., Batalha, N. M., Brown, T. M., Caldwell, D., Christensen-Dalsgaard, J., . . . Hayley, W. (2010). *Kepler mission* design, realized photometric performance, and early science. *The Astrophysical Journal Letters, 713*, L79-86.

Ledoux, P. (1951). The nonradial oscillations of gaseous stars and the problem of beta Canis Majoris. *The Astrophysical Journal, 114*, 373.

Liebert, J., Saffer, R. A., & Green, E. M. (1994). The evolved hot stars of the old, metal-rich galactic cluster NGC 6791. *The Astronomical Journal*, *107*, 1408-21.

Maxted, P. F. L., Heber, U., Marsh, T. R., & North, R. C. (2001). The binary fraction of extreme horizontal branch stars. *Monthly Notices of the Royal Astronomical Society, 326*, 1391-1402.

Miglio, A., Brogaard, K., Stello, D., Chaplin, W. J., D'Antona, F., Montalban, J., Basu S., . . . Kjeldsen, H. (2012). Asteroseismology of old open clusters with Kepler: direct estimate of the integrated red giant branch mass-loss in NGC 6791 and 6819. *Monthly Notices of the Royal Astronomical Society*, *419*, 2077-88.

Mochejska, B. J., Stanek, K. Z., Sasselov, D. D., & Szentgyorgyi, A. H. (2002). Planets in stellar clusters extensive search. I. Discovery of 47 low-amplitude variables in the metal-rich cluster NGC 6791 with millimagnitude image subtraction photometry. *The Astronomical Journal, 123*, 3460-72.

Moni Bidin, C., Moehler, S., Piotto, G., Momany, Y., & Recio-Blanco, A. (2009). A lack of close binaries among hot horizontal branch stars in globular clusters. M 80 and NGC 5986. *Astronomy and Astrophysics, 498*, 737-51.

Østensen, R. H., Green, E. M., Bloemen, S., Marsh, T. R., Laird, J. B., Morris, M., Moriyama, E., . . . Koch, D. G. (2010a). 2M1938+4603: a rich, multimode pulsating sdB star with an eclipsing dM companion observed with *Kepler*. *Monthly Notices of the Royal Astronomical Society, 408*, L51-55.

Østensen, R. H., Silvotti, R., Charpinet, S., Oreiro, R., Hanler, G., Green, E. M., Bloemen, S., . . . Quintana, E. V. (2010b). First *Kepler* results on compact pulsators – I. Survey target selection and the first pulsators. *Monthly Notices of the Royal Astronomical Society, 409*, 1470-86.

Østensen, R. H., Geier, S., Schaffenroth, V., Telting, J. H., Bloemen, S., Nemeth, P., Beck, P. G., . . . Marsh, T. R. (2013). Binaries discovered by the MUCHFUSS project. FBS 0117+396: An sdB+dM binary with a pulsating primary. *Astronomy and Astrophysics, 559*, A35.

Østensen, R. H., Telting, J. H., Reed, M. D., Baran, A. S., Nemeth, P., & Kiaeerad, F. (2014). Asteroseismology revealing trapped modes in KIC 10553698A. *Astronomy and Astrophysics, 569*, A15.

Pablo, H., Kawaler, S. D., & Green, E. M. (2011). Exploring B4: A pulsating sdB star, in a binary, in the open cluster NGC 6791. *The Astrophysical Journal Letters, 740*, L47.

Pesnell, W. D. (1985). Observable quantities of nonradial pulsations in the presence of slow rotation. *The Astrophysical Journal, 292*, 238-48.

Prialnik, D. (2010). *Theory of stellar structure and evolution.* New York, NY: Cambridge UP.

Ramspeck, M., Heber, U., & Edelmann, H. (2001). Early type stars at high galactic latitudes. II. Four evolved B-type stars of unusual chemical composition. *Astronomy and Astrophysics, 379*, 235-44.

Reed, M. D., & Stiening, R. (2004). Using 2MASS to detect main sequence companions to subdwarf B stars. *Astrophysics and Space Science, 291*, 329-32.

Reed, M. D., Baran, A. S., Quint, A. C., Kawaler, S. D., O'Toole, S. J., Telting, J. H., Charpinet, S., . . . Christensen-Dalsgaard, J., and references therein. (2011). First Kepler results on compact pulsators - VIII. Mode identifications via period spacings in g-mode pulsating subdwarf B stars. *Monthly Notices of the Royal Astronomical Society, 414*, 2885-92.

Reed, M. D., Baran, A. S., Østensen, R. H., Telting, J. H., & O'Toole, S. J. (2012). The discovery of two pulsating subdwarf B stars in NGC 6791using *Kepler* data. *Monthly Notices of the Royal Astronomical Society, 427*, 1245-51.

Reed, M. D., Foster, H., Telting, J. H., Østensen, R. H., Farris, L. H., Oreiro, R., & Baran, A. S. (2014). Analysis of the rich frequency spectrum of KIC 10670103 revealing the most slowly rotating subdwarf B star in the *Kepler* field. *Monthly Notices of the Royal Astronomical Society, 440*, 3809-24.

Reed, M. D., Baran, A. S., Østensen, R. H., Telting, J. H., Kern, J. W., Bloemen, S., Blay, P., . . . Rowe, L. (2016). A pulsation analysis of K2 observations of the subdwarf B star PG 1142-037 during Campaign 1: A subsynchronously rotating ellipsoidal variable. *Monthly Notices of the Royal Astronomical Society, 458*, 1417-26.

Salaris, M. (2015). Open Clusters: Probes of galaxy evolution and bench tests of stellar models. In: Miglio A., et al. *Asteroseismology of stellar populations in the Milky Way,* Springer. *Astrophysics and Space Science Proceedings*, *39*, 43-50.

Schindler, J. T., Green, E. M., & Arnett, W. D. (2015). Exploring stellar evolution models of sdB stars using MESA. *The Astrophysical Journal, 806*, 178.

Schuh, S., Huber, J., Dreizler, S., Heber, U., O'Toole, S. J., Green, E. M., & Fontaine, G. (2006). HS 0702+6043: a star showing both short-period p-mode and long-period g-mode oscillations. *Astronomy and Astrophysics, 445*, L31-34.

Stobie, R. S., Kilkenny, D., O'Donoghue, D., Chen, A., Koen, C., Morgan, D. H., Barrow, J., . . . Watson, F. G. (1997). The Edinburgh-Cape blue object survey - I. Description of the survey. *Monthly Notices of the Royal Astronomical Society, 287*, 848-66.

Sweigart, A. V. (1987). Evolutionary sequences for horizontal branch stars. *The Astrophysical Journal Supplement Series, 65*, 95-135.

Telting, J. H., Østensen, R. H., Baran, A. S., Bloemen, S., Reed, M. D., Oreiro, R., Farris, L. H., . . . Kjeldsen, H. (2012). Three ways to solve the orbit of KIC 11558725: a 10-day beaming sdB+WD binary with a pulsating subdwarf. *Astronomy and Astrophysics, 544*, A1.

Unno, W., Osaki, Y., Ando, H., & Shibahashi, H. (1979). *Nonradial oscillations of stars.* Tokyo, Japan: University of Tokyo Press.

Van Cleve, J. E., Christiansen, J., Jenkins, J. M., Caldwell, D. A., Barclay, T., Bryson, S. T., Burke, C. J., . . . Zamudio, K. (2016). *KSCI-19040-005: Kepler data characteristics handbook (KDCH).* Moffett Field, CA: NASA Ames Research Center.

Van Grootel, V., Charpinet, S., Fontaine, G., Brassard, P., & Green, E. (2014). The mass distribution of sdB stars derived by asteroseismology and other means: Implications for stellar evolution theory." *Astronomical Society of the Pacific Conference Series*, *481*, 229.

Vos, J., Østensen, R. H., Nemeth, P., Green, E. M., Heber, U., & Van Winckel, H. (2013). The orbits of subdwarf-B + main-sequence binariesII. Three eccentric systems; BD +29°3070, BD +34°1543 and Feige 87. *Astronomy and Astrophysics, 559*, A54.

Wisotzki, L., Koehler, T., Groote, D., & Reimers, D. (1996). The Hamburg/ESO survey for bright QSOs. I. Survey design and candidate selection procedure. *Astronomy and Astrophysics Supplement, 115,* 227.